Analysis and Simulation of Maxwell's Equations for the Design of 2D Functional Materials

A DISSERTATION
SUBMITTED TO THE FACULTY OF THE GRADUATE SCHOOL
OF THE UNIVERSITY OF MINNESOTA
BY

Jung Heon Song

IN PARTIAL FULFILLMENT OF THE REQUIREMENTS
FOR THE DEGREE OF
DOCTOR OF PHILOSOPHY

Mitchell Luskin & Matthias Maier

July, 2020

Acknowledgements

I would like to take this moment to express my deepest gratitude to my advisors, Prof. Mitchell B. Luskin and Prof. Matthias S. Maier for their continued support and advice throughout this long journey. I would also like to thank them for all the opportunities in regards to research, collaboration, and teaching.

Additionally, I thank my mentors pre-graduate career: Prof. Chris H. Rycroft, Dr. Maciej Haranczyk and Dr. Kesheng John Wu. Prof. Rycroft was the first to open my eyes to the world of applied mathematics and provided me an opportunity to grow as an aspiring computational scientist. I was fortunate enough to spend a year at Lawrence Berkeley National Lab, with the guidance of Dr. Kesheng Wu, at the Scientific Data Management Group. It was during this time I cemented my desire to pursue a doctoral degree, and I express my sincerest gratitude to him for introducing me to an interdisciplinary field of applied mathematics.

On the domestic side, I express my sincerest gratitude to my parents and my brother for their never-ending encouragement and support.

Abstract

This thesis develops numerical frameworks for the simulation of light-guiding structures involving atomically thin 2D materials. Particular electromagnetic waves of interest are the surface plasmon polaritons (SPPs), which are slowly decaying electromagnetic waves that are highly confined to the 2D material. Characterized by subwavelength confinement, effective manipulation of SPPs are of great importance in nanophotonics, and in turn, in the design of an optical wavegudie. To that end, this dissertation studies how to manipulate intrinsic properties of waveguides to control its effectiveness.

In particular, we discuss analytically and numerically the propagation and energy transmission of electromagnetic waves caused by the coupling of SPPs between two spatially separated layers of 2D materials, such as graphene, at subwavelength distances. We construct an adaptive finite element method to compute the distance at which the optimal tranmission is attained.

Next, a more generalized structural setup is laid out by introducing spatially dependent dielectrics and arbitrarily shaped interior conducting interface(s). This leads to a quartic eigenvalue problem with mixed transverse electric (TE) and transverse magnetic (TM) modes, and strongly coupled electric and magnetic fields. We derive a weak formulation of the quartic eigenvalue problem and introduce a numerical solver based on a *quadratification approach*, in which the quartic eigenvalue problem is transformed to a *spectrally equivalent* linear eigenvalue problem. As a practical example, we demonstrate how an improved quality factor (defined by the ratio of the real and the imaginary part of the computed eigenvalues) can be obtained for a family of spatially dependent host materials with internal conducting interfaces. We outline how this result lays the groundwork for solving related shape optimization problems.

Contents

List of Tables

List of Figures

Chapter 1

Introduction

For the past few decades, the field of nanophotonics has undergone a surge of research interest to confine and control light on the subwavelength scale for faster and more efficient methods to communicate data. The fundamental set of equations that govern all electromagnetic phenomena is Maxwell's equations, and it is imperative that fast and efficient numerical solvers be developed for designing integrated optical devices and discovering novel optical phenomena to further advances in photonic techonology. A type of electromagnetic wave with applications in various optical devices is the surface plasmon polariton (SPP).

SPPs are charge density waves that are coupled to electromagnetic waves at the interface between a metal and a dielectric substrate. Exhibiting strong confinement and relatively low propagation losses, they are thought to be a novel way to confine and control light on the subwavelength scale in the field of nanophotonic technology. In the past, noble metals were usually considered the best plasmonic materials due to their relatively low losses in the visible to near-infrared spectrum. Stemming from this finding, a number of SP waveguiding structures were proposed, such as metal films [1], metal groove/wedges [2], metal nanowires [3], and hybrid plasmonic waveguides [4, 5]. These structures, however, are limited by the fact that they only support weakly confined SP waves in the mid-infrared to terahertz frequency regime. Although this particular frequency range has important applications in biology, communication, and spectroscopy, it is not ideal for the development of nanophotonic devices.

Another subject of much interest is graphene, a two-dimensional carbon allotrope with a *single atom layer* that is arranged in a honeycomb lattice structure [6]. It has a wide potential for applications in nanophotonics due to a number of desirable electronic and optical features,

such as extreme confinement, low losses, and extreme tunability [6, 7]. In the infrared regime, the electric surface conductivity of such a 2D material is characterized by being complex-valued with a dominant positive imaginary part. This allows for the propagation of SPPs. Plasmons on graphene offer not only a lower ohmic loss than the conventional plasmonic materials, but also a strong subwavelength confinement of EM fields [8, 4]. The tunability of graphene by electrical gating or chemical doping, in addition, makes graphene a promising candidate for future compact plasmon devices [9]. Graphene surface plasmon waveguiding structures have been investigated intensively. These include graphene surface plasmon modes on a single graphene sheet [10], graphene nanoribbons [11], graphene grooves/wedge waveguides [12], graphene-coated nanowire waveguides [13, 14], and graphene-based cylindrical hybrid waveguides [8]. Several experiments have shown that a graphene layer can tightly coat the dielectric nanowire due to van der Waals force.

Consequently, waveguide structures that enable subwavelength confinement of the optical modes are of great importance in nanophotonics, and in turn, in the design of optimal waveguides. To that end, this dissertation studies how to manipulate intrinsic properties of waveguides to control its effectiveness. We proceed to demonstrate this in a systematic fashion. First, we discuss analytically and numerically the propagation and energy transmission of EM waves caused by the coupling of SPPs between two spatially separated layers of 2D materials, such as graphene, at subwavelength distances. Although some studies that investigated the plasma modes and optical SPP modes of a *double-layer* graphene were published [15, 16, 17], the majority of research on graphene has been on a single-layer systems consisting of a single, planar sheet of graphene [18, 19, 20]. By introducing a second, parallel sheet, placed at a small but finite distance to the other sheet, it is possible to drastically change the confinement and propagation characteristics of SPPs.

Next, we study a quartic eigenvalue problem arising in the context of optical waveguiding problems involving atomically thick 2D materials. The waveguide configuration in consideration consists of a spatially dependent dielectric equipped with conducting interior interfaces. This leads to a quartic eigenvalue problem with mixed transverse electric and transverse magnetic modes, and strongly coupled electric and magnetic fields. Optical properties of cylindrical waveguides with graphene interfaces have been extensively studied in the engineering community [8, 21, 13, 14]. Recently, focus has also shifted to gradient-index structures that

couple with graphene [22, 23]. These structures are based on planar and cylindrical graphene-dielectric multilayer metamaterials, and have shown potential applications in terahertz imaging, sensing, detecting, and communication areas [22, 23]. Numerical methods that compute eigenvalues of inhomogeneously loaded domains have been studied before [24, 25, 26, 27]. A finite difference frequency-domain method is used to analyze eigenmodes of inhomogeneously loaded rectangular waveguides in [24]. Another study [27] presents a method for computing solenoidal eigenmodes and the corresponding eigenvalues of the vector Helmholtz equation. However, neither of these references take into account possible conducting interfaces. On the numerical side, there exist a number of methods for numerically solving nonlinear eigenvalue problems. The FEAST algorithm [28, 29] uses complex contour integration to compute a cluster of eigenvalues within some user-defined region in the complex plane. Studies have also used the algorithm to simulate propagation of light through optical fibers [30, 31]. Another technique is within the context of Rayleigh quotient optimization problems [32], where a nonlinear eigenvalue problem is solved using a spectral transformation based on nonlinear shifting and a reformulation using second-order derivatives. In this thesis, however, a different method based on *quadratification* is proposed that is both pragmatic and applicable to a wide range of optical waveguiding problems.

Objective of the thesis The main goal of this thesis is to present an efficient and reliable numerical setup for the simulation of time harmonic Maxwell's equation with conducting interfaces in the context of optimal optical waveguide design. Though there are commercial softwares available which numerically sovle Maxwell's equations, they are often times neither fast nor accurate. This dissertation attempts to address these issues by investigating particular cases of Maxwell's equations which are relevant in modern optics and optical design. There are a number of parameters that impact the efficiency of a light-guiding structure – the geometry, the type of host material, and the configuration of conducting interfaces, to name a few – and each of them contribute to the overall effectiveness in a nontrivial manner. To that end, this thesis will investigate, both numerically and analytically, how it is possible to utilize each individual parameter's role in the designing of optimal waveguides.

Layout of the thesis This dissertation is organized as follows: Chapter 2 gives an

overview of Maxwell's equations which will form as the basis for the subsequent chapters. Elementary results on existence and uniqueness of Maxwell's equations are presented. The chapter concludes with a discussion of a suitable class of finite element spaces for discretizing the Maxwell system.

In Chapter 3, numerical investigation of an infinite 2D waveguide is laid out by computing a finite element approximation for the solution of the corresponding scattering problem, governed by time-harmonic Maxwell's equations. This prototypical geometry is motivated by proposed waveguide configurations that include graphene layers, or carbon nanotubes as an integral part of their design [33]. By adjusting the confinement of the two-layer system, we find an optimal spacing for which the coupling of the SPPs is maximal. This is achieved using a goal-oriented mesh refinement strategy and a perfectly matched layer. Chapter 4 starts by investigating the analytical aspect of the two-layer system. An integral equation describing the time-harmonic electromagnetic field of a double-layer structure is presented. We examine the contributions from a pole of the scattered field solution, which are responsible for the generation of SPPs. We demonstrate that our findings are in accordance with those from a single-layer system by observing the evolution of the scattered field under different interlayer spacings. The optimal spacing is computed and compared against the value found in Chapter 3.

Chapter 5 introduces a general class of waveguide configurations that consist of a gradient-index host material and contains (arbitrarily shaped) interior conducting 2D material interfaces. This setup stems from recent studies, which proposes effective gradient refractive index structures by tailoring the surface conductivity of the graphene layers to provide a given phase profile along with the structures. Gradient-index devices face a number of limitations in material requirements, which are removed by introducing gradient index metamaterials [34]. Metamaterials are artificial structures that are engineered at a subwavelength scale to obtain naturally unavailable macroscopic properties. Gradient refractive index metamaterials are alloted more freedom to manipulate electromagnetic waves, and consequently, many novel applications and optimized performances such as reconfigurable and high-resolution lenses [35, 36, 37, 38], photonic jets [39, 40, 41], high-performance antenna [42], invisibility cloaks [43], couplers and interconnectors [44, 45], steerers [46, 47] are reported to be based on them.

We derive a variational, nonlinear quartic eigenvalue problem for the waveguiding problem incorporating a gradient-index host material and interior conducting interfaces. The nonlinear quartic character of the eigenvalue problem stems from the fact that the spatially dependent material parameters causes a strong coupling between the otherwise decoupled transverse magnetic (TM) and transverse electric (TE) modes. We solve the quartic eigenvalue problem numerically by transforming it to a spectrally equivalent linear system using a quadratification [48] approach. Additional numerical tools, such as the Möbius transform and a perfectly matched layer (PML) are employed to assist with solving the eigenvalue problem. We verify our numerical method against analytical solutions for prototypical geometries with internal conducting interfaces. As a practical example, we demonstrate how an improved quality factor (defined by the ratio of the real and the imaginary part of the computed eigenvalues) can be obtained (a) for a family of gradient-index host materials, and (b) by deformation of the geometry (see Section 5.5.3). Finally, we outline how our framework lays the groundwork for a related shape optimization problem. A conclusion and future outlook is given in Chapter 6.

Chapter 2

A survey of Maxwell's equations

2.1 Maxwell's Equations

The classical macroscopic electromagnetic field is characterized by four vector functions, $\boldsymbol{E}(\boldsymbol{x})$, $\boldsymbol{D}(\boldsymbol{x})$, $\boldsymbol{H}(\boldsymbol{x})$ and $\boldsymbol{B}(\boldsymbol{x})$. $\boldsymbol{E}$ and $\boldsymbol{H}$ denote the electric and magnetic field, respectively, and $\boldsymbol{D}$ and $\boldsymbol{B}$ are called the electric displacement and magnetic induction. Maxwell's equations describe the relationship between these vector functions, which are laid out below:

$$\begin{cases} \dfrac{\partial \boldsymbol{B}(\boldsymbol{x})}{\partial t} + \nabla \times \boldsymbol{E} = -\boldsymbol{M}_a(\boldsymbol{x}), \\ \nabla \cdot \boldsymbol{D} = \rho, \\ \dfrac{\partial \boldsymbol{D}(\boldsymbol{x})}{\partial t} - \nabla \times \boldsymbol{H} = -\boldsymbol{J}_a(\boldsymbol{x}), \\ \nabla \cdot \boldsymbol{B} = \rho_m, \end{cases} \tag{2.1}$$

where $\boldsymbol{J}_a(\boldsymbol{x})$ and $\boldsymbol{M}_a(\boldsymbol{x})$ are externally applied, electric current, and magnetic-current densities, respectively. ρ is an electric charge density, and ρ_m is correspondingly a magnetic charge density. The first equation of (2.1) is Faraday's law, which describes a spatially varying electric field always accompanies a time-varying magnetic field. The third equation of (2.1) is Ampère's law, which relates the integrated magnetic field around a closed loop to the electric current passing through the loop. Combined with the Gauss's law for the electric field and the magnetic field, the four set of equations constitutes Maxwell's equations. Although $\boldsymbol{M}_a$ and ρ_m do not occur in nature, we include them here to demonstrate the duality of the two

fields. $\boldsymbol{E}$ and $\boldsymbol{H}$ are related to $\boldsymbol{D}$ and $\boldsymbol{B}$, respectively, by the constitutive relation

$$\begin{cases} \boldsymbol{D}(\boldsymbol{x}) = \varepsilon(\boldsymbol{x})\boldsymbol{E}(\boldsymbol{x}), \\ \boldsymbol{B}(\boldsymbol{x}) = \mu(\boldsymbol{x})\boldsymbol{H}(\boldsymbol{x}). \end{cases} \tag{2.2}$$

Here, $\mu(\boldsymbol{x})$ and $\varepsilon(\boldsymbol{x})$ are complex-valued rank 2 tensor quantities, where $\mu(\boldsymbol{x})$ denotes the magnetic permeability and $\varepsilon(\boldsymbol{x})$ denotes the electric permittivity. In the frequency domain, the time-dependent problem can be reduced to the time-harmonic Maxwell system. In that case, the (constant) temporal frequency $\omega > 0$ is introduced to the solution fields, i.e., all vector-valued components $\mathscr{F}$ have the form

$$\mathscr{F}(\boldsymbol{x}, t) = \mathrm{Re}\big(e^{-i\omega t}\,\mathscr{F}(\boldsymbol{x})\big). \tag{2.3}$$

Time-harmonic Maxwell's equations with an electric current density then read [49, 50]:

$$\begin{cases} -i\omega\,\boldsymbol{B}(\boldsymbol{x}) + \nabla\times\boldsymbol{E}(\boldsymbol{x}) = -\boldsymbol{M}_a(\boldsymbol{x}), \\ \nabla\cdot\boldsymbol{B}(\boldsymbol{x}) = \dfrac{1}{i\omega}\nabla\cdot\boldsymbol{M}_a(\boldsymbol{x}), \\ i\omega\,\varepsilon(\boldsymbol{x})\boldsymbol{E}(\boldsymbol{x}) + \nabla\times\big(\mu(\boldsymbol{x})^{-1}\boldsymbol{B}(\boldsymbol{x})\big) = \boldsymbol{J}_a(\boldsymbol{x}), \\ \nabla\cdot\big(\varepsilon(\boldsymbol{x})\boldsymbol{E}(\boldsymbol{x})\big) = \dfrac{1}{i\omega}\nabla\cdot\boldsymbol{J}_a(\boldsymbol{x}). \end{cases} \tag{2.4}$$

We assume a general $\boldsymbol{x}$ dependence of all quantities with some (weak) regularity conditions to ensure unique solvability that will be stated later. We are interested in simulating waveguide configurations that feature reasonably arbitrarily shaped conducting interface(s). The discontinuity along the surface due to the conductivity leads to a set of jump conditions [51, 49, 7, 52]:

$$\begin{cases} [\nu\times\boldsymbol{H}]_\Sigma = \sigma^\Sigma\boldsymbol{E}_T, \\ [\nu\cdot\mu\boldsymbol{H}]_\Sigma = 0, \\ [\nu\times\boldsymbol{E}]_\Sigma = 0, \\ [\nu\cdot\varepsilon\boldsymbol{E}]_\Sigma = \dfrac{1}{i\omega}\nabla\cdot(\sigma^\Sigma\boldsymbol{E}), \end{cases} \tag{2.5}$$

where ν is a chosen unit normal vector field on Σ, and $[\,.\,]_\Sigma$ denotes the jump over Σ with respect to ν, viz.,

$$[\boldsymbol{F}]_\Sigma(\boldsymbol{x}) := \lim_{\alpha\searrow 0}\Big(\boldsymbol{F}(\boldsymbol{x}+\alpha\nu) - \boldsymbol{F}(\boldsymbol{x}-\alpha\nu)\Big) \qquad \boldsymbol{x}\in\Sigma.$$

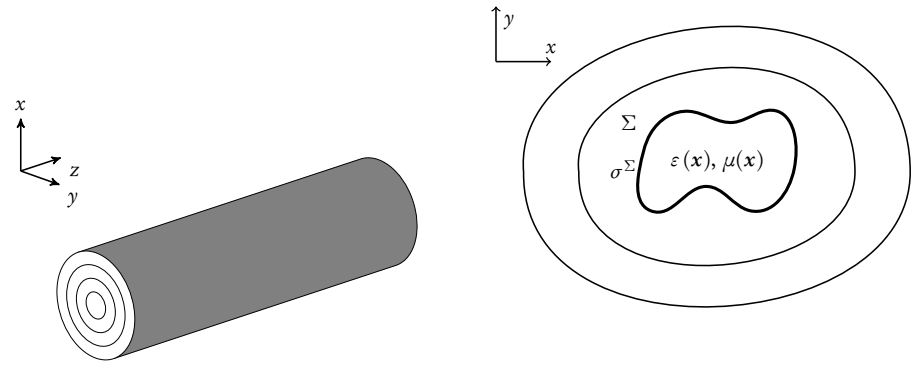

(a) (b)

Figure 2.1: (a) Schematic of a prototypical multilayer waveguide. (b) Cross-sectional schematic of the computational domain. The closed curve, Σ, is prescribed with a non-vanishing conductivity, $\sigma^{\Sigma}(\boldsymbol{x})$. The waveguide is characterized by material parameters $\varepsilon(\boldsymbol{x})$ and $\mu(\boldsymbol{x})$.

We also fix the notation

$$\boldsymbol{F}^{+} := \lim_{\alpha \searrow 0} \boldsymbol{F}(\boldsymbol{x}+\alpha\boldsymbol{\nu}), \quad \boldsymbol{F}^{-} := \lim_{\alpha \searrow 0} \boldsymbol{F}(\boldsymbol{x}-\alpha\boldsymbol{\nu}), \quad \text{for } \boldsymbol{x} \in \Sigma,$$

and the subscript T denotes the tangential part of the respective vector, $\mathscr{F}_T = (\boldsymbol{\nu} \times \mathscr{F}) \times \boldsymbol{\nu}$. Under appropriate conditions on $\sigma(\boldsymbol{x})$, jump condition (2.5) generates SPPs on the interface [53, 7]. In this formalism, (2.4)(b), (2.4)(d), (2.5)(b) and (2.5)(d) are redundant.

We make the assumption that $\varepsilon(\boldsymbol{x})$ and $\mu(\boldsymbol{x})$ become homogeneous and isotropic for large $|\boldsymbol{x}|$ and impose the Silver-Müller radiation condition at infinity [52], viz.,

$$\lim_{|x|\to\infty} \{\boldsymbol{B} \times \boldsymbol{x} - c^{-1}|\boldsymbol{x}|\boldsymbol{E}\} = 0, \quad \lim_{|x|\to\infty} \{\boldsymbol{E} \times \boldsymbol{x} + c|\boldsymbol{x}|\boldsymbol{B}\} = 0, \quad \boldsymbol{x} \notin \Sigma. \tag{2.6}$$

Here, $c = 1/\sqrt{\varepsilon\,\mu}$ denotes the speed of light in the respective medium. The explicit inclusion of this condition is omitted in our numerical simulation by incorporating appropriate boundary conditions or an arbitrary perfectly matched layer (PML), see 3.2.2 and 5.3.2.

Although it is possible to derive numerical schemes for the first-order system in (2.4), it is more often convenient to eliminate the magnetic field $\boldsymbol{B}$ by substituting (2.4)(c) into (2.4)(a) to obtain the second-order equation

$$\nabla \times (\mu^{-1} \nabla \times \boldsymbol{E}) - \omega^2 \varepsilon \boldsymbol{E} = i\omega \boldsymbol{J}_a - \nabla \times (\mu^{-1} \boldsymbol{M}_a). \tag{2.7}$$

For the computational domain Ω, an absorbing boundary condition at $\partial\Omega$ can be imposed. A popular choice is

$$\nu \times \boldsymbol{B} + \sqrt{\mu^{-1}\,\varepsilon}\,\boldsymbol{E}_T = 0, \qquad \text{for } x \in \partial\Omega, \tag{2.8}$$

which is a first-order approximation of the Silver-Müller radiation condition (2.6) truncated at $\partial\Omega$ [54]. This will be referred to as the first-order absorbing boundary condition [52]. We assume that both μ and ε are scalar functions at the boundary or in the neighborhood of the boundary such that the square root in (2.8) is well-defined.

In the later sections, it will prove to be useful to introduce a rescaling to reduce the time-harmonic Maxwell system into a dimensionless equations. For now, however, we will work with the unscaled system.

2.2 Solution theory of the time-harmonic Maxwell's equations

Assume that the domain $\Omega \subset \mathbb{R}^3$ is bounded, simply connected and Lipschitz-continous with piecewise smooth boundary, $\partial\Omega$. Assume also that Σ is a connected Lipschitz-continuous, piecewise smooth boundary with nonvanishing conductivity. Multiply (2.7) with the complex conjugate of a test function φ and subsequent integration by parts over $\Omega\backslash\Sigma$ yields

$$\begin{aligned}\int_\Omega (\mu^{-1}\nabla\times\boldsymbol{E})\cdot(\nabla\times\overline{\varphi})\,\mathrm{d}x - \int_\Omega \omega^2\varepsilon\,\boldsymbol{E}\cdot\overline{\varphi}\,\mathrm{d}x \\ - \int_\Sigma [\nu\times(\mu^{-1}\nabla\times\boldsymbol{E} + \mu^{-1}\boldsymbol{M}_a)]_\Sigma\cdot\overline{\varphi}_T\,\mathrm{d}o_x \\ + \int_{\partial\Omega} (\nu\times(\mu^{-1}\nabla\times\boldsymbol{E} + \mu^{-1}\boldsymbol{M}_a))\cdot\overline{\varphi}_T\,\mathrm{d}o_x \\ = i\omega\int_\Omega \boldsymbol{J}_a\cdot\overline{\varphi}\,\mathrm{d}x - \int_\Omega \mu^{-1}\boldsymbol{M}_a\cdot\nabla\times\overline{\varphi}\,\mathrm{d}x,\end{aligned} \tag{2.9}$$

for $\varphi \in X(\Omega) = \{\varphi \in \boldsymbol{H}(\mathrm{curl};\Omega) : \varphi_T|_\Sigma \in L^2(\Sigma)^3, \varphi_T|_{\partial\Omega} \in L^2(\partial\Omega)^3\}$, where the space $\boldsymbol{H}(\mathrm{curl};\Omega)$ denotes the subspace of $L^2(\cdot)^3$ consisting of square integrable functions whose (distributive) curl admits a representation by a square integrable function.

The jump condition over the conducting sheet can be expressed as a weak discontinuity. Rewriting (2.5) and (2.8) in terms of $\boldsymbol{B}$ and $\boldsymbol{M}_a$ yields

$$[\nu\times(\mu^{-1}\nabla\times\boldsymbol{E} + \mu^{-1}\boldsymbol{M}_a)]_\Sigma = i\omega\,\sigma^\Sigma\boldsymbol{E}_T \qquad \text{on } \Sigma, \tag{2.10}$$

$$\nu\times(\mu^{-1}\nabla\times\boldsymbol{E} + \mu^{-1}\boldsymbol{M}_a) = -i\sqrt{\mu^{-1}\,\varepsilon}\,\boldsymbol{E}_T \qquad \text{on } \partial\Omega. \tag{2.11}$$

These two expressions allow us to enforce the jump and the boundary conditions weakly by a simple substitution, which can be summarized as follows: find $\boldsymbol{E} \in \boldsymbol{X}(\Omega)$ such that

$$A(\boldsymbol{E}, \varphi) = F(\varphi), \tag{2.12}$$

for all $\varphi \in \boldsymbol{X}(\Omega)$, where the sesquilinear form and the right-hand side are given by

$$\begin{aligned} A(\boldsymbol{E}, \varphi) &:= \int_\Omega (\mu^{-1} \nabla \times \boldsymbol{E}) \cdot (\nabla \times \overline{\varphi}) \, \mathrm{d}x - \int_\Omega \omega^2 \varepsilon \, \boldsymbol{E} \cdot \overline{\varphi} \, \mathrm{d}x \\ &\quad - i\omega \int_\Sigma \sigma^\Sigma \boldsymbol{E}_T \cdot \overline{\varphi}_T \, \mathrm{d}o_x - \int_{\partial\Omega} \sqrt{\mu^{-1} \varepsilon} \, \boldsymbol{E}_T \cdot \overline{\varphi}_T \, \mathrm{d}o_x, \\ F(\varphi) &:= i\omega \int_\Omega \boldsymbol{J}_a \cdot \overline{\varphi} \, \mathrm{d}x - \int_\Omega \mu^{-1} \boldsymbol{M}_a \cdot \nabla \times \overline{\varphi} \, \mathrm{d}x. \end{aligned} \tag{2.13}$$

Now, we will present relevant theorems that guarantee the existence and uniqueness of (2.12).

Proposition 2.2.1. *(cf. [55] Th. 2.3) Assume for simplicity that μ and $\sqrt{\mu^{-1}\varepsilon}$ are positive, real, scalar constants, ε and σ^Σ are measurable complex-valued functions satisfying*

$$\begin{aligned} 0 < c \le Im\, \varepsilon(\boldsymbol{x}) \le C \quad \text{and} \quad |Re\, \varepsilon(\boldsymbol{x})| \le C \quad \forall \boldsymbol{x} \in \Omega, \\ 0 < c \le \frac{1}{d} Re\, \sigma^\Sigma(\boldsymbol{x}) \le C \quad \text{and} \quad \left| \frac{1}{d} Im\, \sigma^\Sigma(\boldsymbol{x}) \right| \le C \quad \forall \boldsymbol{x} \in \Sigma, \end{aligned} \tag{2.14}$$

for some constants c and C. Then the system (2.12) *has a unique solution in $\boldsymbol{X}(\Omega)$ for all $\boldsymbol{J}_a$ and $\boldsymbol{M}_a \in L^2(\Omega; \mathbb{C}^3)$, where*

$$\boldsymbol{X} = \{\varphi \in H(curl; \Omega; \mathbb{C}^3) : \ \varphi_T \in L^2(\partial\Omega; \mathbb{C}^3), \ \varphi_T \in L^2(\Sigma; \mathbb{C}^3)\}.$$

Proposition 2.2.2. *(cf. [49] Th. 4.12) Assume that the coefficients ε and μ are piecewise smooth. Assume additionally that Ω may be decomposed into P subdomains denoted Ω_p, $p = 1, \ldots, P$ such that*

- *$\overline{\Omega} = \bigcup \overline{\Omega}_p$, where $\overline{\Omega}$ demotes the closure of Ω;*
- *$\Omega_p \cap \Omega_q = \emptyset$, if $p \neq q$;*
- *each subdomain Ω_p is connected and has a Lipschitz boundary;*
- *the coefficient μ is constant on each subdomain*
- *the coefficient ε has the properties*

- $\varepsilon\big|_{\Omega_p} \in H^3(\Omega_p)$;
- *there is a constant* $c > 0$ *such that for each* p, *either* $Im(\varepsilon) \geq c$ *on* Ω_p *or* $Im(\varepsilon) = 0$ *on* Ω_p.

Then there is at most one solution $\boldsymbol{E}$ *to* (2.12) *for* $\boldsymbol{E} \in \boldsymbol{X}$, *where* $\boldsymbol{X}$ *is defined as above.*

The proof makes use of Fredholm's alternative to deal with noncoercivity of the sesquilinear form.

2.3 Finite element spaces for time-harmonic Maxwell's equations

The curl operator has a large null space, which must be removed from $\boldsymbol{X}$ via the Helmholtz decomposition. Let $\boldsymbol{X}_0$ be a subspace of $\boldsymbol{X}$ with the null space of the curl operator removed from $\boldsymbol{X}$. From the Helmholtz decomposition, it is natural to consider a class of finite element space that lie in the space $\boldsymbol{X}_0$. Use of standard continuous piecewise liniear finite elements, which are in $(H^1(\Omega))^3$, cannot, in general, be successful without special modification due to the fact that $(H^1(\Omega))^3 \cap \boldsymbol{X}_0$ is a proper subset of $\boldsymbol{X}_0$ when Ω has re-entrant corners [49]. Hence, the resulting finite element space is too large as the mesh size goes to zero [56, 57, 58, 59]. This non-conformity complicates the analysis and implementation of finite element methods for Maxwell's equations [49].

To remedy this issue, finite elements suitable for discretizing the energy space for electromagnetics are needed, i.e., Nédélec edge elements [60]. To analyze Nédélec edge elements, other families of elements are needed to discretize $H(\mathrm{div};\Omega)$ and $L^2(\Omega)$. This relation is summarized by the following de Rham diagram [61, 62]:

$$
\begin{array}{ccccccc}
H^1(\Omega) & & H(\mathrm{curl};\Omega) & & H(\mathrm{div};\Omega) & & L^2(\Omega) \\
\cup & & \cup & & \cup & & \cup \\
C^\infty & \xrightarrow{\nabla} & (C^\infty)^3 & \xrightarrow{\nabla\times} & (C^\infty)^3 & \xrightarrow{\nabla\cdot} & C^\infty \\
\downarrow{\scriptstyle \pi_h} & & \downarrow{\scriptstyle \boldsymbol{r}_h} & & \downarrow{\scriptstyle \boldsymbol{w}_h} & & \downarrow{\scriptstyle P_{o,h}} \\
U_h & \xrightarrow{\nabla} & V_h & \xrightarrow{\nabla\times} & W_h & \xrightarrow{\nabla\cdot} & Z_h
\end{array}
\tag{2.15}
$$

where U_h, V_h, W_h and Z_h are finite element spaces which are contained in $H^1(\Omega)$, $H(\mathrm{curl};\Omega)$, $H(\mathrm{div};\Omega)$ and $L^2(\Omega)$, respectively. $\pi_h, \boldsymbol{r}_h, \boldsymbol{w}_h$ and $P_{o,h}$ describe interpolation operators that

map from suitable subspaces into the appropriate finite element spaces. In summary, the diagram implies that given a smooth enough $p \in U \subset H^1(\Omega)$, then $\nabla \pi_h p = r_h \nabla p$. The commutability that follows from the de Rham diagram is the existence of an approximate Helmholtz decomposition of a vector field into the gradient of a scalar potential and an almost divergence-free vector. The finite element spaces U_h, V_h, W_h, and Z_h relate to vertex, edge, face, and volume, respectively. Here, W_h is the Nédélec-Raviart-Thomas space in 3D. This connects to the finite element exterior calculus [63].

2.3.1 The curl conforming edge elements of Nédélec

A finite element is said to be conforming in $H(\text{curl})$ if given two elements K_1 and K_2, with a common face f, and $u \in (C^\infty(\overline{K_1 \cup K_2}))^3$, the functions v defined by $v = \Pi_1 u$ on K_1 and $v = \Pi_2 u$ on K_2 belong to $H(\text{curl}, K_1 \cup K_2)$, where Π_i is the interpolant operator.

Proposition 2.3.1. *(cf. [60] Lemma 6) A finite element is conforming in $H(curl)$ if and only if The tangential components of $\Pi_1 u$ and $\Pi_2 u$ are the same of f.*

We will now introduce a finite element space developed by Nédélec. We first present necessary polynomial spaces to construct Nédélec's edge elements. We assume that the domain Ω is coverred with a mesh of regular parallelepipeds of maximum diameter h to form the mesh τ_h. Given a multi-index α, a polynomial $p \in P_k$ iff it can be written as

$$p(x) = \sum_{|\alpha|_1 \leq k} a_\alpha x^\alpha,$$

for some choice of coefficients $a_\alpha \in \mathbb{C}$. Similarly, a polynomial $\tilde{p} \in \tilde{P}_k$ iff

$$\tilde{p}(x) = \sum_{|\alpha|_1 = k} a_\alpha x^\alpha,$$

for some choice of coefficients $a_\alpha \in \mathbb{C}$. Let S_k be a subspace of homogeneous vector polynomials of degree k, given by

$$S_k = \left\{ p \in (\tilde{P}_k)^3 : x \cdot p = 0 \right\}.$$

Now define R_k by

$$R_k = (P_{k-1})^3 \oplus S_k.$$

This space is a quite natural space of polynomials for a Helmholtz decomposition of $(P_k)^3$, since it can be seen that

$$(P_k)^3 = R_k \oplus \nabla \tilde{P}_{k+1}.$$

Proposition 2.3.2. *(cf. [60] Thm 5) Define a finite element space (K, R_k, Σ_K) where*

- *K is a hexahedron.*
- *The degrees of freedom, Σ_K, are of three types associated with edges e, faces f, and K. The three different degrees of freedom are defined as follows:*

$$M_e(\boldsymbol{u}) = \left\{ \int_e \boldsymbol{u} \cdot \tau q \, ds \quad \forall q \in P_{k-1}(e) \text{ for each edge } e \text{ of } K \right\},$$

$$M_f(\boldsymbol{u}) = \left\{ \int_f \boldsymbol{u} \times \boldsymbol{\nu} \cdot \boldsymbol{q} \, dA \quad \forall \boldsymbol{q} \in Q_{k-2,k-1}(f) \times Q_{k-1,k-2}(f) \text{ for each face } f \text{ of } K \right\},$$

$$M_K(\boldsymbol{u}) = \left\{ \int_K \boldsymbol{u} \cdot \boldsymbol{q} \, dV \quad \text{for all } \boldsymbol{q} \in Q_{k-1,k-2,k-2} \times Q_{k-2,k-1,k-2} \times Q_{k-2,k-2,k-1} \right\},$$

where τ is the unit vector directed along the edge e and $Q_{l,m,n}$ are the polynomials in three variables, the maximum degree of which are respectively l, m, and n.

Then this finite element space is unisolvent and conforming in the Hilbert space $H(curl)$.

The immediate consequence of using this finite element space is that we immediately get well-posedness of (2.14) with $\boldsymbol{E} \in \boldsymbol{X}_h(\Omega)$, provided that $h \leq h_0$ [49].

Chapter 3

Direct numerical simulation of waveguide configurations

The SPP dispersion of a single graphene layer and a single graphene layer deposited on dielectric substrates has been extensively investigated by many authors [64, 18, 20]. Additional confinement and a change of propagation characteristics can be achieved by stacking another layer of these 2D materials on top of a single-layer [65]. By extension, theoretical aspects of bilayer graphene [17, 66, 15], multilayer graphene [67], and intercalated graphite [68] have been studied recently.

However, a rigorous numerical and analytical treatment of waveguide configurations involving time-harmonic Maxwell's equations is not of primary interests in these publications. This chapter aims to address three points. First, we introduce a reliable and efficient numerical method to readily compute propagation characteristics of the SPPs in a double-layer structure. Second, we validate the numerical findings against an analytical solution. Third, we demonstrate that our numerical approach is easily extensible to different computational domains.

3.1 Variational formulation

In this section, we lay out the variational formulation for time-harmonic Maxwell's equations with an interface condition. We introduce a rescaling for time-harmonic Maxwell's equations that will ease the numerical computation of SPPs [52].

3.1.1 Rescaling and variational formulation

Numerical values in SI units for solutions of (2.4) are many orders of magnitude apart. Further, the typical length scale of SPP is one to two orders of magnitude smaller than the free-space wavelength k_0 [7]. These discrepancies in the magnitude of the length scales makes the direct numerical simulation of the SPPs difficult. As a remedy we use a rescaling to dimensionless units that normalizes the length scale by the free-space wavenumber, k_0, [52]:

$$\begin{gathered}
\boldsymbol{x} \to k_0 \boldsymbol{x}, \quad \nabla \to \frac{1}{k_0}\nabla, \quad \mu \to \mu_r = \frac{1}{\mu_0}\mu, \\
\varepsilon \to \varepsilon_r = \frac{1}{\varepsilon_0}\varepsilon, \quad \sigma \to \sigma_r^{\Sigma} = \sqrt{\frac{\mu_0}{\varepsilon_0}}\sigma. \quad \boldsymbol{J}_a \to \boldsymbol{J}_a = \frac{1}{J_0}\boldsymbol{J}_a, \\
\boldsymbol{M}_a \to \boldsymbol{M}_a = \frac{k_0}{\omega\mu_0 J_0}\boldsymbol{M}_a, \quad \boldsymbol{E} \to \boldsymbol{E} = \frac{k_0^2}{\omega\mu_0 J_0}\boldsymbol{E}, \quad \boldsymbol{B} \to \boldsymbol{B} = \frac{k_0}{J_0}\mu^{-1}\boldsymbol{B}.
\end{gathered}$$

Here, ε_0 and μ_0 denote the vacuum permittivity and permeability, respectively. This leads to two distinctly separated scales: one related to the free-space wavenumber ~ 1, and another for the SPP wavenumber, $k_{\mathrm{SPP}} \sim 1/\sigma_r^{\Sigma}$, on the conducting sheets [52]. The rescaled, dimensionless form of time-harmonic Maxwell's equation (2.4) reads

$$\begin{cases}
-i\mu_r(\boldsymbol{x})\boldsymbol{B}(\boldsymbol{x}) + \nabla \times \boldsymbol{E}(\boldsymbol{x}) = -\boldsymbol{M}_a(\boldsymbol{x}), \\
\nabla \cdot (\mu_r(\boldsymbol{x})\boldsymbol{B}(\boldsymbol{x})) = \frac{1}{i}\nabla \cdot \boldsymbol{M}_a(\boldsymbol{x}), \\
i\varepsilon_r(\boldsymbol{x})\boldsymbol{E}(\boldsymbol{x}) + \nabla \times \boldsymbol{B}(\boldsymbol{x}) = \boldsymbol{J}_a(\boldsymbol{x}), \\
\nabla \cdot \big(\varepsilon_r(\boldsymbol{x})\boldsymbol{E}(\boldsymbol{x})\big) = \frac{1}{i}\nabla \cdot \boldsymbol{J}_a(\boldsymbol{x}).
\end{cases} \tag{3.1}$$

The rescaled jump conditions (2.5) are

$$\begin{cases}
\big[\boldsymbol{\nu} \times (\mu_r^{-1}\boldsymbol{B})\big]_{\Sigma} = \sigma_r \boldsymbol{E}_T, \\
[\boldsymbol{\nu} \cdot \boldsymbol{B}]_{\Sigma} = 0, \\
[\boldsymbol{\nu} \times \boldsymbol{E}]_{\Sigma} = 0, \\
[\boldsymbol{\nu} \cdot \varepsilon_r \boldsymbol{E}]_{\Sigma} = \frac{1}{i}\nabla \cdot (\sigma_r^{\Sigma}\boldsymbol{E}),
\end{cases} \tag{3.2}$$

the rescaled Silver-Müller radiation condition (2.6) reads

$$\boldsymbol{\nu} \times \boldsymbol{B} + \sqrt{\mu_r^{-1}\varepsilon_r}\,\boldsymbol{E}_T = 0 \qquad (\boldsymbol{x} \in \partial\Omega), \tag{3.3}$$

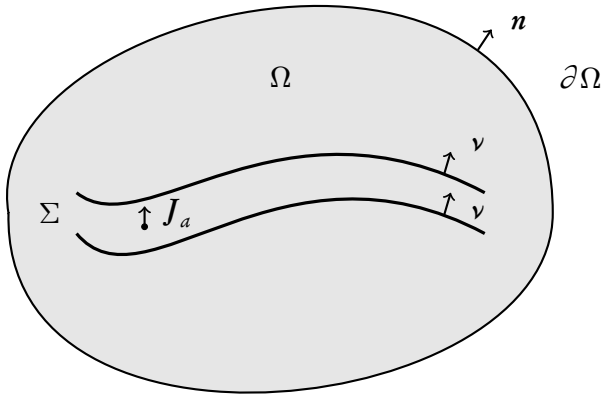

Figure 3.1: Schematic of the computational domain, Ω, with boundary $\partial\Omega$, outer normal $\boldsymbol{n}$, and normal field $\boldsymbol{\nu}$ defined on the waveguide Σ. An electric Hertzian dipole, $\boldsymbol{J}_a$, is placed inside a prescribed waveguide structure, Σ.

and the corresponding second-order Maxwell system (2.7) is given by

$$\nabla \times \left(\mu_r^{-1} \nabla \times \boldsymbol{E}\right) - \varepsilon_r \boldsymbol{E} \;=\; i\,\boldsymbol{J}_a - \nabla \times \left(\mu_r^{-1} \boldsymbol{M}_a\right). \tag{3.4}$$

Multiplying (3.4) with the complex conjugate of a test function φ and subsequent integration by parts using (3.2) and (3.3) recovers the corresponding weak formulation:

$$A(\boldsymbol{E}, \varphi) \;=\; i \int_\Omega \boldsymbol{J}_a \cdot \bar{\varphi}\, \mathrm{d}x \;-\; \int_\Omega \mu_r^{-1} \boldsymbol{M}_a \cdot \nabla \times \varphi\, \mathrm{d}x, \tag{3.5}$$

for $\varphi \in \boldsymbol{X}(\Omega) = \{\varphi \in \boldsymbol{H}(\mathrm{curl};\Omega) : \varphi_T|_\Sigma \in L^2(\Sigma)^3, \varphi_T|_{\partial\Omega} \in L^2(\partial\Omega)^3\}$ and with the bilinear form

$$\begin{aligned} A(\psi, \varphi) = \int_\Omega (\mu_r^{-1} \nabla \times \psi) \cdot (\nabla \times \bar{\varphi}) - (\varepsilon_r\, \psi) \cdot \bar{\varphi}\; \mathrm{d}x \\ - i \int_\Sigma (\sigma_r^\Sigma \psi_T) \cdot \bar{\varphi}\, \mathrm{d}o_x \;- i \int_{\partial\Omega} \sqrt{\mu_r^{-1}\, \varepsilon_r}\, \psi_T \cdot \bar{\varphi}\, \mathrm{d}o_x. \end{aligned} \tag{3.6}$$

Equation (3.5) will serve as a starting point for a finite element discretization. Elementary results on existence and uniqueness were discussed in 2.2.

Remark. *In the 2D version of Maxwell's equations with a vertical electric dipole (see Section 4.1), the Magnetic field, $\boldsymbol{B}$, is given by [52]*

$$\boldsymbol{B} = \mu_r^{-1}(\boldsymbol{M}_a + \nabla \times \boldsymbol{E}), \quad \boldsymbol{M}_a \equiv 0, \tag{3.7}$$

is a scalar function when viewed as a vector field in $\mathbb{R}^3$. Additionally, for the remainder of this section, it will be assumed that the magnetic current density, $\boldsymbol{M}_a \equiv 0$.

3.2 Numerics: Computational domain and discretization scheme

In this section, we discuss a direct numerical simulation approach that efficiently computes the SPPs and plasmonic interactions on a two-layer system. A PML is introduced and its role in negating the undesired effects of the absorbing boundary condition of the plasmon modes is described. Additionally, a local adaptive mesh refinement strategy is presented that captures the highly oscillatory behaviors of the plasmons near the interfaces. The variational formulation (3.5) is discretized on a non-uniform quadrilateral mesh with higher-order, curl-conforming Nédélec elements [69]. Such a choice is ideal where the weak jump condition is naturally treated by aligning with the mesh. Let $\boldsymbol{X}_h(\Omega) \subset \boldsymbol{X}(\Omega)$ be a finite element subspace spanned by Nédélec elements. Then under a sufficiently refined initial mesh, the variational formulation

$$A(\boldsymbol{E}_h, \varphi) = i \int_\Omega \boldsymbol{J}_a \cdot \bar{\varphi} \, \mathrm{d}x.$$

is uniquely solvable for $\boldsymbol{E}_h \in \boldsymbol{X}_h(\Omega)$ and for all $\varphi \in \boldsymbol{X}_h(\Omega)$.

3.2.1 Prototypical waveguide configuration

We will study a prototypical geometry consisting of two flat, conducting layers in a square domain. The two layers are arranged parallel to each other with distance d apart; see Figure 3.2. This prototypical geometry is motivated by proposed waveguide configurations that include for example concentrically arranged carbon nanotubes as integral part of their design [33] (see Figure **??**. Even though our waveguide configuration is quite simple in comparison, we make the claim that due to the dominance of the SPP interaction of the two layers we actually capture the quantitative behavior of the two-layer interaction quite well. Our computational framework has thus the potential of guiding the design of more complicated waveguide structures in the future.

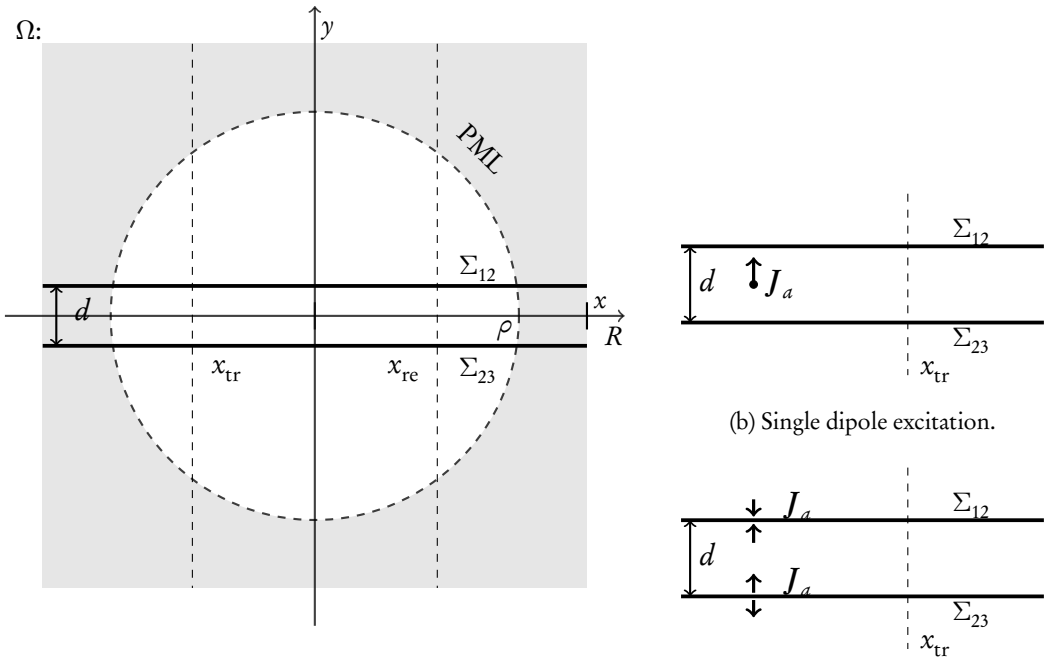

(a) The computational domain. The location of the Hertzian dipole(s) is shown in the right.

(b) Single dipole excitation.

(c) Double dipole excitation.

Figure 3.2: The computational domain Ω (a), together with the two different current source configurations (b, c) used in the numerical computations. The energy transmission ratio is computed by measuring $\boldsymbol{E}_T^2$ at $x = x_{\text{tr}}$ and $x = x_{\text{re}}$.

Two different current sources are considered: a single vertical Hertzian dipole placed at the midpoint of the two sheets (see Figure 3.2b); and a double dipole configuration with one dipole placed directly on each sheet (see Figure 3.2c). The use of such dipole sources in order to excite the desired SPP modes in the waveguide configuration is again an idealization. However, due to the large magnitude of the excited SPP modes, the influence of the dipole is neglibible already after a short distance from the source. Only the dominant travelling mode is observed, which enables us to study essentially "free" coupled SPP structures in the waveguide.

In the numerical computation we regularize dipoles to a small but finite thickness. This necessitates a change of sign in the double dipole configuration when crossing over the interface Σ. See Section 5.5.1 for details. In the case of the double dipole excitation, the proximity of the sources to the interface renders the SPP mode that is excited to dominate [51]. For the

single dipole excitation, however, the strength of the SPP vanishes exponentially with the distance d. For this reason, we will primarily focus on numerical results obtained with double dipole excitation, 2(b).

The values x_{tr} and x_{re} are the transmission and reception locations, respectively, at which the tangential component of the energy is to be measured. In principle, a number of choices for the quantity of interest, $\mathscr{J}(\boldsymbol{E})$, are possible. In the following, we use a non-linear quantity of interest given by an *energy transmission ratio*:

$$\mathscr{J}(\boldsymbol{E}) = \frac{\int_{-R}^{R} \cos^2\left(\frac{\pi y}{2R}\right) |\boldsymbol{E}_T|^2(x = x_{\mathrm{re}}, y)\,\mathrm{d}y}{\int_{-R}^{R} \cos^2\left(\frac{\pi y}{2R}\right) |\boldsymbol{E}_T|^2(x = x_{\mathrm{tr}}, y)\,\mathrm{d}y}. \tag{3.8}$$

The numerator computes the transmitted energy, measured at a vertical strip located sufficiently far from the source, and the denominator calculates the received energy. The integrands in $\mathscr{J}(\boldsymbol{E})$ are modified by weight functions that localize the integral to a vertical strip where we measure the field intensity for transmission and reception. The choice (3.8) for the quantity of interest leads to a localized right-hand side $\mathscr{J}$ of the dual problem that is sensitive to the highly oscillatory SPPs associated with the electric field, $\boldsymbol{E}$.

Remark. *The functional $\mathscr{J}(\boldsymbol{E})$ is continuously differentiable as long as the denominator is different from zero. This is indeed the case for the solution $\boldsymbol{E}$ and all approximations $\boldsymbol{E}_h$ for our choice of geometry and dipole excitation.*

3.2.2 Perfectly Matched Layer

A perfectly matched layer (PML) is a truncation procedure motivated from *electromagnetic* scattering problem in the time domain. The underlying idea of a PML is to surround the computational domain with an artificial *sponge* layer such that all outgoing electromagnetic waves decay exponentially with minimal artificial reflection [70, 71, 49].

As outlined in [52, 49], we carry out a change of coordinates from the computational domain with real-valued coordinates to a domain with complex-valued coordinates. Projecting back to the real coordinates yields again system (2.4) with (3.2), but with *modified* material parameters $(\varepsilon_r, \mu_r^{-1}, \sigma_r^{\Sigma})$ *inside* the PML. We refer the reader to [52] for details.

The PML can be implemented by suitably replacing $(\varepsilon_r, \mu_r^{-1}, \sigma_r^{\Sigma})$ within the PML. For a

spherical absorption layer we define the matrices

$$A = T_{e_x e_r}^{-1}\,\mathrm{diag}\Big(\frac{1}{\bar{d}^2}, \frac{1}{d\,\bar{d}}, \frac{1}{d\,\bar{d}}\Big)T_{e_x e_r}, \quad B = T_{e_x e_r}^{-1}\,\mathrm{diag}\big(d, \bar{d}, \bar{d}\big)T_{e_x e_r}, \tag{3.9}$$
$$C = T_{e_x e_r}^{-1}\,\mathrm{diag}\Big(\frac{1}{\bar{d}}, \frac{1}{\bar{d}}, \frac{1}{d}\Big)T_{e_x e_r},$$

$$d = 1 + i\,s(r), \quad \bar{d} = 1 + i/r \int_\rho^r s(\tau)\,\mathrm{d}\tau. \tag{3.10}$$

Here, r denotes the distance to the origin, $s(\tau)$ is an appropriate nonnegative scaling function that will be defined later, $T_{e_x e_r}$ is the rotation matrix that rotates $\boldsymbol{e}_r$ onto $\boldsymbol{e}_x$. The material parameters are hence transformed inside the PML as follows:

$$\begin{cases} \mu_r^{-1} & \longrightarrow \quad B\,\mu_r^{-1}\,A, \\ \varepsilon_r & \longrightarrow \quad A^{-1}\,\varepsilon_r\,B^{-1}, \\ \sigma_r^{\Sigma} & \longrightarrow \quad C^{-1}\,\sigma_r^{\Sigma}\,B^{-1}. \end{cases} \tag{3.11}$$

3.2.3 A posteriori error estimation and local refinement

One of the computational challenges of our problem is the need for a much finer mesh refinement near the interfaces Σ_{12} and Σ_{23} in order to resolve all small scale SPP structures. We discuss now an efficient adaptive refinement scheme utilizing an a posteriori error estimator based on the *dual weighted residual* (DWR) method [72].

Consider the following *dual* problem: Find a solution $\boldsymbol{Z} \in \boldsymbol{H}(\mathrm{curl};\Omega)$ such that

$$\int_\Omega \Big[(\mu_r^{-1}\nabla\times\boldsymbol{\varphi})\cdot(\nabla\times\bar{\boldsymbol{Z}}) - \varepsilon_r\,\boldsymbol{\varphi}\cdot\bar{\boldsymbol{Z}}\Big]\,\mathrm{d}x \tag{3.12}$$
$$-\int_\Sigma \sigma_r^{\Sigma}\boldsymbol{\varphi}_T\cdot\bar{\boldsymbol{Z}}\,\mathrm{d}o_x + \int_{\partial\Omega}\sqrt{\mu_r^{-1}\,\varepsilon_r}\,\boldsymbol{\varphi}\cdot\bar{\boldsymbol{Z}}\,\mathrm{d}o_x = D_E\mathscr{J}(E)[\boldsymbol{\varphi}],$$

for all $\boldsymbol{\varphi} \in \boldsymbol{X}(\Omega)$, where $\mathscr{J}(E)$ is a *quantity of interest* mapping

$$\mathscr{J} : \boldsymbol{H}(\mathrm{curl};\Omega) \to \mathbb{C}. \tag{3.13}$$

The dual solution $\boldsymbol{Z}$ *encodes* how the target error quantity depends on local properties of the data [72]. Next, we define *local error indicators* with the help of the solutions $\boldsymbol{E}$ and $\boldsymbol{Z}$ of the primal problem (3.5) and dual problem (3.12), respectively [52], [72, Prop. 2.1]:

$$\big|\mathscr{J}(\boldsymbol{E}) - \mathscr{J}(\boldsymbol{E}_h)\big| \le \sum_{Q\in\mathbb{T}_H}\eta_Q + R, \quad \text{with} \quad \eta_Q := \frac{1}{2}\Big|\rho_Q + \rho_Q^*\Big|. \tag{3.14}$$

Here, ρ_Q and ρ_Q^* denote the primal and dual cell-wise residual, respectively, associated with variational equations (3.5) and (3.12):

$$\rho_Q = i\int_\Omega \boldsymbol{J}_a \cdot \big((\bar{\boldsymbol{Z}}-\bar{\boldsymbol{Z}}_h)\chi_Q\big)\,\mathrm{d}x - A\big(\boldsymbol{E}_h,(\boldsymbol{Z}-\boldsymbol{Z}_h)\chi_Q\big), \tag{3.15}$$

$$\rho_Q^* = \mathrm{D}_E\mathscr{J}(\boldsymbol{E}_h)[(\boldsymbol{E}-\boldsymbol{E}_h)\chi_Q] - A\big((\boldsymbol{E}-\boldsymbol{E}_h)\chi_Q,\boldsymbol{Z}_h\big), \tag{3.16}$$

where $A(\,.\,)$ is given in (3.6). Here, χ_Q denotes the indicator function associated to Q, that is, $\chi_Q(\boldsymbol{x})$ is 1 inside the cell Q, and 0 otherwise. The local error indicator η_Q given by (3.14) can now be approximated and used in a local refinement strategy [72].

Remark. *The remainder term R is cubic in the error $||E-E_h||$ and can therefore generally be neglected [72]. More precisely, for our particular choice of quantity of interest* (3.8) *a lengthy calculation reveals*

$$\begin{aligned}|R| &= \Big|\frac{1}{2}\int_0^1 \mathrm{D}_E^3\mathscr{J}(\boldsymbol{E}_H + s(\boldsymbol{E}-\boldsymbol{E}_H))[\boldsymbol{E}-\boldsymbol{E}_h]^3 s(s-1)\mathrm{d}s\Big| \\ &\lesssim \Big(\frac{1}{R}\int_{-R}^{R}\cos^2\big(\frac{\pi y}{2R}\big)|\boldsymbol{E}_T|^2(x=x_{\mathrm{tr}},y)\,\mathrm{d}y\Big)^{-3}\big\|\boldsymbol{E}-\boldsymbol{E}_h\big\|^3,\end{aligned}$$

provided that the numerator in (3.8) is smaller than the denominator (which is true for our choice of geometry). Given the fact that we place the measurement position x_{tr} close to the source we conclude that $|R|$ is well controlled and small in our case.

Our goal is an optimal local refinement for the numerical simulation of energy propagation of the SPPs at the location of our choosing. Consequently, the *weight* $\boldsymbol{Z}-\boldsymbol{Z}_h$ in residual (3.15) is generally large near the interface and at points where the influence of the solution on quantity (3.8) is high.

In practice, the numerical evaluation of (3.15) and (3.16) is typically done with the use of a higher-order approximation for the dual solution $\boldsymbol{Z}$ and the primal solution $\boldsymbol{E}$. However, such a calculation of a higher-order approximation is computationally costly. We therefore use a patch-wise projection $\pi_{2H}^{(2)}\boldsymbol{Z}_h$ to a higher-order space on a coarser mesh level [73]:

$$\boldsymbol{Z}-\boldsymbol{Z}_h \approx \pi_{2H}^{(2)}\boldsymbol{Z}_h - \boldsymbol{Z}_h, \quad \boldsymbol{E}-\boldsymbol{E}_h \approx \pi_{2H}^{(2)}\boldsymbol{E}_h - \boldsymbol{E}_h. \tag{3.17}$$

3.3 Direct numerical simulation

In this section we present computational results for the two-layer system that was introduced above. We demonstrate numerically how the (effective) wavenumber of SPP structures depends on the interlayer distance d and investigate the functional relationship of the energy transmission ratio to the interlayer distance d. We determine the optimal spacing, which will later be used to compare against the analytical findings from Section 4.1. We validate our local refinement strategy by comparing the convergence rates with uniform refinement, and demonstrate the effectiveness of the numerical tools discussed in Section 5.3. All numerical computations are carried out with the finite element library deal.II [74, 75].

3.3.1 Setup and discretization parameters

We consider a vertical electric dipole positioned at $\boldsymbol{a}_1 = (-0.7, 0)$ (for single dipole excitation), and at $\boldsymbol{a}_{2/3} = (-0.7, \pm d/2)$ (for the double dipole excitation). The current density $\boldsymbol{J}_a$ is thus given by

$$\boldsymbol{J}_a = \begin{pmatrix} 0 \\ J_0 \end{pmatrix} \delta(\boldsymbol{x} - \boldsymbol{a}_1), \text{ and } \qquad \boldsymbol{J}_a = \begin{pmatrix} 0 \\ J_0 \end{pmatrix} \big(\delta_2(\boldsymbol{x} - \boldsymbol{a}_2) + \delta_3(\boldsymbol{x} - \boldsymbol{a}_3)\big), \tag{3.18}$$

for single, or double dipole excitation, respectively. We use two values for the surface conductivities, $\sigma^{\Sigma}_{r,12} = \sigma^{\Sigma}_{r,23} = \sigma^{\Sigma}_r$,

$$\sigma^{\Sigma}_r = 0.002 + 0.2i, \text{ and } 0.002 + 0.15i,$$

that are within realistic parameter ranges [52]. The computational domain, Ω, is chosen to be a square with edge length 4. A spherical PML is enforced for $\rho > 1.6$. Following [49, 52], we regularize the Dirac deltas in the current density as follows,

$$\delta_i(\boldsymbol{x} - \boldsymbol{a}_i) \approx \frac{\operatorname{sgn}\Big((y - \frac{d}{2})(-y - \frac{d}{2})\Big) \cos^2\Big(\frac{\pi}{(2\, r_d)} \|(\boldsymbol{x} - \boldsymbol{a}_i)\|_2\Big)}{\Big(\frac{\pi}{2} - \frac{2}{\pi}\Big)\, r_d^2},$$

for $\|\boldsymbol{x} - \boldsymbol{a}_i\|_2 < r_d$, and 0 otherwise. The signum function ensures that the regularized dipole changes sign whenever the regularization crosses the conducting layer Σ_{12}, or Σ_{23}. We choose a fixed value of $r_d = 10 \cdot 2^{-12}$ throughout the paper. We set the position at which we evaluate (3.8) to $x_{\text{tr}} = -0.65$ and $x_{\text{re}} = 0.75$. This choice maximizes the distance $|x_{\text{re}} - x_{\text{tr}}|$ while ensuring

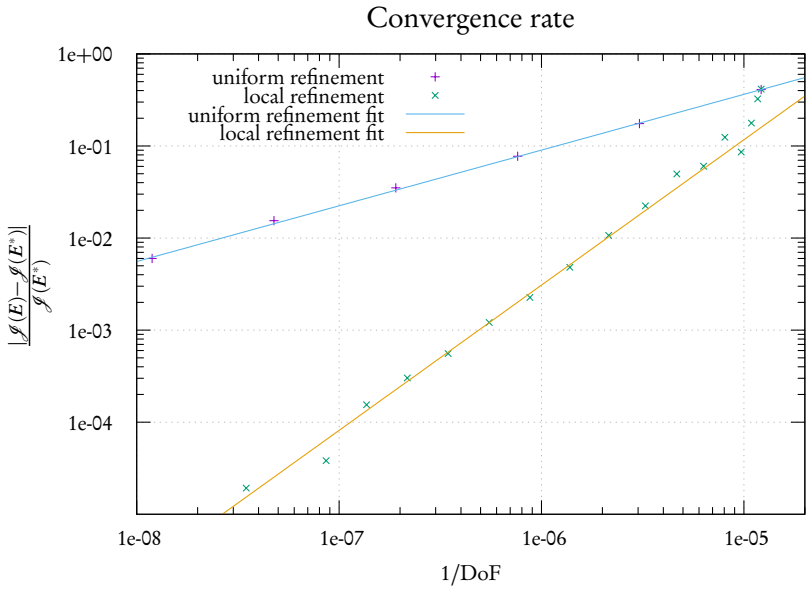

Figure 3.3: Convergence of the energy tranmission ratio for uniform and local refinement for $d = 0.20$. The relative error of the transmission ratios obtained with both refinement strategies, respectively, are plotted against the inverse of the number of degrees of freedom. We observe a convergence order of about $c \approx 0.6$ for uniform refinement and $c \approx 1.6$ for local refinement. The reference value $\mathscr{J}E^*$ was obtained by taking a weighted average of the asymptotic transmission ratios, c_{local} and c_{uniform}.

that evaluation points are sufficiently far away from the regularized dipole sources and the PML.

We use the following scaling function $s(\rho)$ for the PML [52]

$$s(\rho) = s_0 \frac{(\rho - 0.8R)^2}{(R - 0.8R)^2}, \tag{3.19}$$

and set the free parameter to $s_0 = 0.05$ in our computations.

3.3.2 Validation of local refinement strategy

We validate our numerical framework by comparing values for the quantity of interest (3.8) obtained by extrapolating numerical values under uniform, and under local refinement. The computations were performed for $d = 0.20$. The results are shown in Figure 3.3. The data is

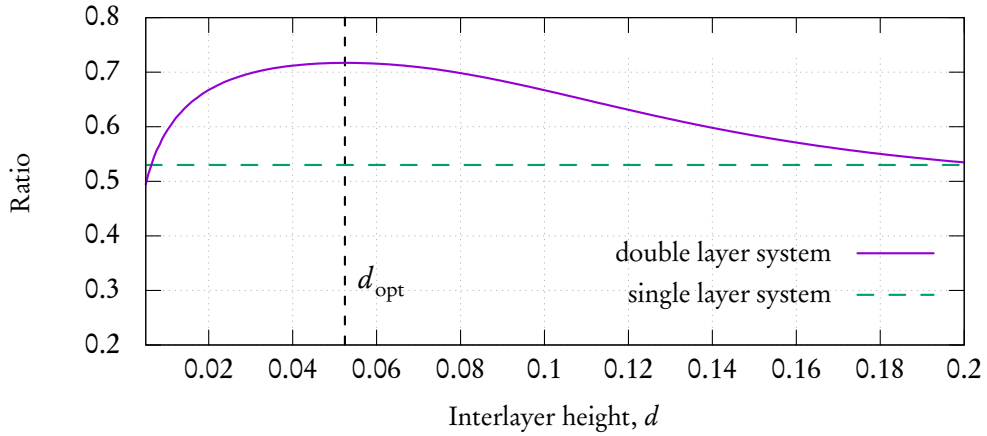

Figure 3.4: Energy transmission ratio as a function of interlayer spacing d computed for the case $\sigma = 0.002 + 0.2i$. The computed optimal spacing for a maximal energy transmission ratio is at $d_{\text{opt}} = 0.05245$. The dashed horizontal line is the energy transmission ratio computed for the control case of a single-layer sheet. For large d, the energy transmission ratio of the two-layer system approaches the value for the single-layer control case asymptotically.

fitted to the curve $f(x) = a + b\,x^c$ and extrapolated. For local refinement, the fit parameters we obtain are $a_{\text{local}} = 0.205333$, $b_{\text{local}} = 1.25229 \times 10^8$, $c_{\text{local}} = 1.57811$, whereas for uniform refinement we get $a_{\text{unif}} = 0.206216$, $b_{\text{unif}} = 85.8656$, $c_{\text{unif}} = 0.612326$. As expected [52], we obtain a much faster convergence rate ($c \approx 1.6$) in the quantity of interest for local refinement as opposed to uniform refinement ($c \approx 0.6$). We conclude that our computation of the energy transmission ratio with $\mathscr{J}(\boldsymbol{E}) \approx a_{\text{local}}$ is reliable within 1%.

3.3.3 Optimal spacing

Next, we preform a parameter study of the energy transmition ratio for varying interlayer spacing d ranging from $d_{\text{min}} = 4 \cdot 10^{-12}$ to $d_{\text{max}} = 0.2$, where d_{max} corresponds to about 1/3 of the single-layer SPP wavelength, $2\pi/\text{Re}(k_{m,r})$, or 1/30 of the free space wavelength [52]. The (interpolated) results are shown in Figure 3.4. We used a releatively coarse initial mesh for all computations with around 20 thousand degrees of freedom. After 12 local refinement cycles using the adaptive refinement procedure outlined in Section 3.2.3, we reached roughly 2 million degrees of freedom on the finest mesh. We make a qualitative comparison of three representative cases: Figure 3.5 shows the real part of the computed scattered electric field

(a) Single-layer control case.

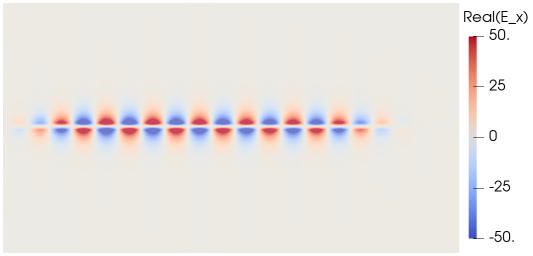

(b) Two-layer configuration with $d = d_{\text{opt}}$

(c) Two-layer configuration with $d \approx 0.18$.

Figure 3.5: Plasmons observed in different configurations, with $\sigma_r^{\Sigma} = 0.002 + 0.2i$. The wavenumber of the excited SPPs in the two-layer case (b) with $d = d_{\text{opt}} \approx 0.05245$ is roughly twice as large as the one obtained in the single-layer control case (a), or the two-layer configuration (b) with large spacing $d \approx 0.18$. The strong interlayer coupling for $d = d_{\text{opt}}$ in (b) results in a much higher SPP amplitude.

in x-direction, $\text{Re}(E_x^{\text{sc}})$, for SPPs on a single-layer system, and a two-layer system with $d = d_{\text{opt}} = 0.05245$ and $d = 0.1805$, respectively. In the case of optimal spacing, $d = d_{\text{opt}}$, the wavenumber of the excited SPPs is roughly twice as large as the one obtained for the single-layer case, cf. Figures 3.5a and 3.5b. For large enough d, for example $d \approx 0.18$, we observe that the wavenumber of the excited SPP approaches the single-layer case, cf. Figures 3.5a and 3.5c. This indicates that the two-layer system is converging to the single-layer setting, analogous to the behavior observed for the energy transmission ratio.

Chapter 4

Analytic solution of an infinite two-layer system

For certain geometries, as presented in Chapter 3, it is possible to construct analytic solutions of Maxwell's equations by systematically solving them [51]. We investigate the field equations in the Fourier space and recognize that the contribution of a certain pole in the complex plane is intrinsically related to the SPP of TM polarization of plane waves.

By focusing on a simple, yet nontrivial model with conducting films, we are able to derive closed-form expressions which explicitly separate the primary field of the dipole, produced in the absence of the conducting layers, from the scattered field. This approach shows how the SPP related to TM polarization can dominate propagation in cases of physical and practical interest.

4.1 Analytic solution and validation

In this section, we derive an analytic solution for (2.4) and (2.5) for an (idealized) infinite two-layer system with single dipole excitation; see Figure 3.2b and Figure 4.1). We identify the limiting behavior for the case of large interlayer spacing d, compute the effective wavenumber of the dominant SPP mode and validate our numerical findings with these results.

For better readability and ease of comparison [51], we revert back from the rescaled version (3.4) to the original form of Maxwell's equations (2.4). Let us consider two planar sheets

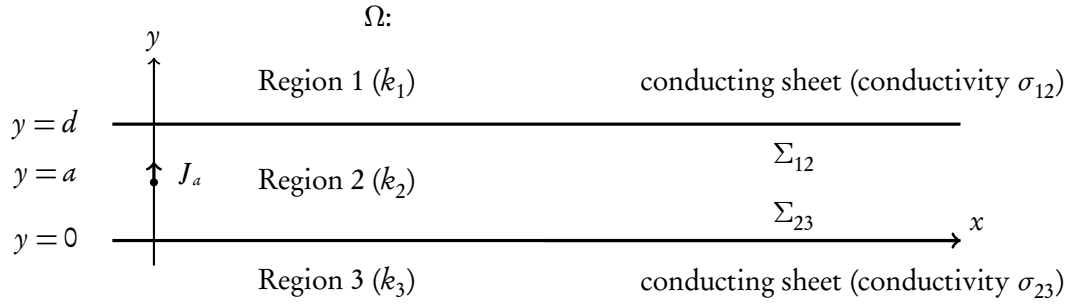

Figure 4.1: Schematic of a vertical electric dipole at a distance a from conducting sheet Σ_{23} in 2D. The dipole has a current density $\boldsymbol{J}_a = J_0\delta(x)\delta(y-a)\boldsymbol{e}_y$. The bottom sheet lies on $y = 0$ and the top sheet lies on $y = d$. Sheets separate the space into region 1 ($\{y > d\}$) with wavenumber k_1, region 2 ($\{0 < y < d\}$) with wavenumber k_2, and region 3 ($\{y < 0\}$) with wavenumber k_3. Each sheet is prescribed with a surface conductivity σ_{12} and σ_{23}, respectively.

in $\mathbb{R}^2$ situated at $y = 0$ and $y = d$, respectively; see Figure 4.1. The conducting sheets separate $\mathbb{R}^2$ into three regions: Region 1 ($\{y > d\}$) has wavenumber k_1 and shares the boundary with region 2 ($\{0 < y < d\}$), whose wavenumber is given by k_2. Region 3 ($\{y < 0\}$) shall have wavenumber k_3, where $k_j^2 = \omega^2\varepsilon_j\mu$. Here, ε_j denotes a complex-valued permittivity ($j = 1,2,3$). Let a vertical electric Hertzian dipole be positioned at $(0,a)$ in between the interfaces, viz., $\boldsymbol{J}_a = \delta(x)\delta(y-a)\boldsymbol{e}_y$. Define the Fourier transform, $\hat{\boldsymbol{F}}(\xi,y)$ of the vector-valued fields ($\boldsymbol{F} \equiv \boldsymbol{B},\boldsymbol{E}$) through the integral formula

$$\boldsymbol{F}(x,y) = \frac{1}{2\pi}\int_{\mathbb{R}} d\xi\, \hat{\boldsymbol{F}}(\xi,y)e^{i\xi x}. \tag{4.1}$$

Applying the Fourier transform to Maxwell's equations (2.4) gives

$$\begin{cases} -i\xi\hat{E}_{jy} + \dfrac{\partial}{\partial y}\hat{E}_{jx} = -i\omega\hat{B}_{jz}, \\ -\dfrac{\partial}{\partial y}\hat{B}_{jz} = \dfrac{ik_j^2}{\omega}\hat{E}_{jx}, \\ -i\xi\hat{B}_{jz} = -\dfrac{ik_j^2}{\omega}\hat{E}_{jy} + \mu\delta(y). \end{cases} \tag{4.2}$$

A number of elementary algebraic manipulations of (4.2) yield the differential equation

$$\left(\frac{\partial^2}{\partial y^2} + \beta_j^2\right)\hat{B}_{jz} = -i\xi\mu\delta(y), \tag{4.3}$$

where we have set $\beta_j^2 = k_j^2 - \xi^2$. We now make the following solution ansatz for the magnetic field obeying the Sommerfeld radiation condition [51]:

$$\hat{B}_{jz}(\xi, y) = \begin{cases} a_1 e^{i\beta_1 y}, & y > d, \\ a_2 e^{i\beta_2 y} + b_2 e^{-i\beta_2 y} - \frac{\xi\mu}{2\beta_2} e^{i\beta_2|y-a|}, & 0 < y < d, \\ b_3 e^{-i\beta_3 y}, & y < 0. \end{cases} \tag{4.4}$$

The remaining electric field components can be derived from the relations

$$\hat{E}_{jx} = \frac{i\omega}{k_j^2}\frac{\partial}{\partial y}\hat{B}_{jz},$$
$$\hat{E}_{jy} = \frac{\omega}{k_j^2 \xi}\left(\xi^2 \hat{B}_{jz} - i\xi\mu\delta(y)\right).$$

Next, we determine closed expressions for the coefficients in (4.4) by matching with boundary conditions (2.5) on each interface:

$$a_1 = \frac{\beta_2 k_1^2}{\beta_1 k_2^2}\left[a_2 e^{i\beta_2 d} - b_2 e^{-i\beta_2 d} - \frac{\xi\mu}{2\beta_2} e^{i\beta_2(d-a)}\right] e^{-i\beta_1 d},$$
$$a_2 = -\frac{\xi\mu}{2\beta_2}\frac{R_{23}(e^{i\beta_2 a}) + R_{12}e^{i\beta_2(2d-a)})}{1 - R_{12}R_{23}e^{2i\beta_2 d}},$$

$$b_2 = -\frac{\xi\mu}{2\beta_2}\frac{R_{12}e^{i\beta_2 d}(e^{i\beta_2(d-a)} + R_{23}e^{i\beta_2(d+a)})}{1 - R_{12}R_{23}e^{2i\beta_2 d}},$$
$$b_3 = -\frac{\beta_2 k_3^2}{\beta_3 k_2^2}\left[a_2 - b_2 + \frac{\xi\mu}{2\beta_2} e^{i\beta_2 a}\right].$$

Here, the constants $R_{ij,m}$ are given by

$$R_{ij} = \frac{\beta_i k_j^2 - \beta_j k_i^2 + \omega\mu\sigma_{ij}\beta_i\beta_j}{\beta_i k_j^2 + \beta_j k_i^2 + \omega\mu\sigma_{ij}\beta_i\beta_j}. \tag{4.5}$$

By substituting back into (4.4) and undoing the Fourier transform, all field components of $\boldsymbol{E}$ and $\boldsymbol{B}$ can be expressed as analytic integrals. In particular, we are interested in $E_{2x}(x, y)$, the electric field component in x-direction between the two-layers:

$$E_{2x}(x, y) = \frac{\omega\mu}{4\pi k_2^2}\int_{-\infty}^{\infty} d\xi \;\; \xi\Bigg[\frac{R_{23}(e^{i\beta_2 a} + R_{12}e^{i\beta_2(2d-a)})}{1 - R_{12}R_{23}e^{2i\beta_2 d}} e^{i\beta_2 y} \\ - \frac{R_{12}e^{2i\beta_2 d}(e^{-i\beta_2 a} + R_{23}e^{i\beta_2 a})}{1 - R_{12}R_{23}e^{2i\beta_2 d}} e^{-i\beta_2 y} + \operatorname{sgn}(y-a)e^{i\beta_2|y-a|}\Bigg] e^{i\xi x}. \tag{4.6}$$

4.1.1 Approximation of the pole contribution

Next, we obtain the scattered electric field in x-direction, E_{2x}^{sc}, observed at $y=0$ by subtracting the incident field

$$\frac{\omega\mu}{4\pi k_2^2}\int_{-\infty}^{\infty} d\xi\ \xi\,\mathrm{sgn}(y-a)e^{i\beta_2|y-a|}e^{i\xi x}.$$

from (4.6). Some additional minor rearrangement yields

$$E_{2x}^{\mathrm{sc}}(x,0)=\frac{\omega\mu}{4\pi k_2^2}\int_{-\infty}^{\infty} d\xi\ \ \xi\Big[\frac{R_{23}e^{i\beta_2 a}}{1-R_{12}R_{23}e^{2i\beta_2 d}}-\frac{R_{12}e^{i\beta_2(2d-a)}}{1-R_{12}R_{23}e^{2i\beta_2 d}} - \frac{R_{12}R_{23}e^{2i\beta_2 d}(e^{i\beta_2 a}-e^{-i\beta_2 a})}{1-R_{12}R_{23}e^{2i\beta_2 d}}\Big]e^{i\xi x} =: \mathrm{(I)}+\mathrm{(II)}+\mathrm{(III)}. \tag{4.7}$$

Each term of the integrand contains SPP contributions stemming from different conducting sheets: Term (I) and (II) arise from the SPP situated at Σ_{23} and Σ_{12}, respectively. Term (III) is a *mixed* term due to the interlayer coupling of SPPs.

We now discuss the role of simple poles in the evaluation of integral (4.7). For the sake of simplicity, let us now assume that $k\equiv k_1=k_2=k_3$ and $\sigma\equiv\sigma_{23}=\sigma_{12}$. Thus, $R_{12}=R_{23}\equiv R$ and $\beta_j\equiv\beta$, where

$$R:=\frac{\omega\mu\sigma\beta}{(2k^2+\omega\mu\sigma\beta)},\qquad \beta^2:=k^2-\xi^2. \tag{4.8}$$

Waveguide modes correspond to *single poles* of the integrand in integral (4.7) [51]. Inspecting (4.7) we see that these are exactly given by the condition $Re^{i\beta d}=\pm 1$. The solution for the branch with the plus sign recovers even waveguide modes, and, correspondingly, the minus sign recovers odd waveguide modes [76].

For d sufficiently small, there is only a single dominant mode. We analyze this case further. The common prefactor of term (I) and (II) is given by

$$\frac{R}{1-R^2e^{2i\beta d}}=\frac{(2k^2+\omega\mu\sigma\beta)\omega\mu\sigma\beta}{(2k^2+\omega\mu\sigma\beta(1-e^{i\beta d}))(2k^2+\omega\mu\sigma\beta(1+e^{i\beta d}))}. \tag{4.9}$$

The TM surface plasmon corresponds to the residue contribution to the electromagnetic field from the pole $\xi=k_m^B$, where k_m^B is a solution of the transcendental relationship for the mode,

$2k^2+\omega\mu\sigma\beta(1-e^{i\beta d})=0$ [51]. Now,

$$2k^2+\omega\mu\sigma\beta(1-e^{i\beta d})\approx -(\xi-k_m^B)(id)k_m^B\omega\mu\sigma\left(e^{i\beta_p d}-\frac{1-e^{i\beta_p d}}{id\beta_p}\right). \tag{4.10}$$

Here, the subscript p denotes evaluation at the pole. Each of I, II, III consists of the branch-cut contribution and the pole contribution. We omit the discussion of the branch-cut in this paper and focus only on the simple pole, $\xi=k_m^B$. This is because for an infinite conducting sheet, the SPP is identified with the part of the electromagnetic field equal to the contribution to the Fourier integrals of the simple pole that solves the above transcendental relationship. For a more thorough discussion on the branch-cut and its computation, we refer readers to [52]. By the residue theorem,

$$\begin{aligned}(\mathrm{I}) &= \frac{\omega\mu}{4\pi k^2}\int_{-\infty}^{\infty} d\xi\ \ \xi\frac{Re^{i\beta a}e^{i\xi x}}{1-R^2e^{2i\beta d}} = (\mathrm{I})^p+(\mathrm{I})^{b.c.};\\ (\mathrm{I})^p &\approx -\frac{i\omega\mu\beta_p^2}{2k^2}\frac{2k^2+\omega\mu\sigma\beta_p}{2k^2+\omega\mu\sigma\beta_p(1+e^{i\beta_p d})}\frac{e^{i(k_m^B x+\beta_p a)}}{1-e^{i\beta_p d}(1+i\beta_p d)}.\end{aligned} \tag{4.11}$$

And similarly for the second integrand term,

$$\begin{aligned}(\mathrm{II}) &= -\frac{\omega\mu}{4\pi k^2}\int_{-\infty}^{\infty} d\xi\ \ \xi\frac{Re^{i\beta(2d-a)}e^{i\xi x}}{1-R^2e^{2i\beta d}} = (\mathrm{II})^p+(\mathrm{II})^{b.c.};\\ (\mathrm{II})^p &\approx \frac{i\omega\mu\beta_p^2}{2k^2}\frac{2k^2+\omega\mu\sigma\beta_p}{2k^2+\omega\mu\sigma\beta_p(1+e^{i\beta_p d})}\frac{e^{i(k_m^B x+\beta_p(2d-a))}}{1-e^{i\beta_p d}(1+i\beta_p d)}.\end{aligned} \tag{4.12}$$

The interlayer pole contribution is calculated in the same fashion.

$$\begin{aligned}(\mathrm{III}) &= -\frac{\omega\mu}{4\pi k^2}\int_{-\infty}^{\infty} d\xi\ \ \xi\frac{R^2e^{2i\beta d}(e^{i\beta a}-e^{-i\beta a})}{1-R^2e^{2i\beta d}}e^{i\xi x} = (\mathrm{III})^p+(\mathrm{III})^{b.c.};\\ (\mathrm{III})^p &\approx \frac{\omega\mu\beta_p^3}{k^2}\frac{\omega\mu\sigma\sin(\beta_p a)}{2k^2+\omega\mu\sigma\beta_p(1+e^{i\beta_p d})}\frac{e^{i(k_m^B x+2\beta_p d)}}{1-e^{i\beta_p d}(1+i\beta_p d)}.\end{aligned} \tag{4.13}$$

4.1.2 Limiting behavior and effective SPP wavenumber

For $d\gg 1$ and fixed dipole position a, we expect the solution of the double-layer system to approach the solution of the single-layer system. We justify this claim by observing that as

$d \to \infty$,

$$
\begin{aligned}
(\mathrm{I})^p \to -\frac{i\omega\mu}{2k^2}\beta_p^2 e^{i(\beta_p a + k_m^B x)} &= -\frac{i\omega\mu}{2k^2}\frac{4k^4}{(\omega\mu\sigma)^2} e^{i(\beta_p a + k_m^B x)} \\
&= -2i\omega\mu\left(\frac{k}{\omega\mu\sigma}\right)^2 e^{ik_m^B x - 2iak^2/(\omega\mu\sigma)},
\end{aligned} \tag{4.14}
$$

which corresponds to the single-layer solution [52]. Further, the remaining terms $(\mathrm{II})_p$ and $(\mathrm{III})_p$ converge to zero due to the presence of $e^{i\beta_p d}$. Under the rescaling introduced in Section 3.1, equation (4.9) becomes

$$
2\mu_r\varepsilon_r + \sigma_r^{\Sigma}\beta_{p,r}(1 - e^{i\beta_{p,r}d_r}) = 0, \text{ with } \beta_{p,r} = \sqrt{\mu_r\varepsilon_r - (k_{m,r}^B)^2}. \tag{4.15}
$$

We numerically solve the above via a root finding algorithm and plot the real and the imaginary part of the wavenumber $k_{m,r}^B$ as a function of distance d_r; see Figure 4.2. For d_r small, $\mathrm{Im}(k_{m,r}^B)$ is greater than the single-layer counterpart. However, upon entering a regime where the interlayer coupling dominates, i.e., where $k_{m,r}^B$ becomes less lossy than $k_{m,r}^M$, we observe that there is an optimal distance, $d_r^{\mathrm{opt}} \approx 0.05538$, at which the scattered field solution in the x-direction attains its maxium. For d_r large enough, only the contribution from the bottom interface remains (term $(\mathrm{II})_p$ and $(\mathrm{III})_p$ vanish), and the wavenumber converges to that of the single-layer case.

4.1.3 Comparison and validation of numerical results

Finally, we compare the numerical results obtained in Section 3.3 to the analytical solution derived above.

In particular, we expect to observe that the contribution from the interlayer coupling term $(\mathrm{III})^p$ of the SPP dominates in the energy transmission ratio. In this vein, our direct numerical simulation is performed for the double-dipole excitation on the interfaces so that the $(\mathrm{III})^p$ dominates [52]; see Section 3.3. We postulate that the complex-valued wavenumber $k_{m,r}^B$ given by (4.15) and associated with the SPP mode $(\mathrm{III})^p$ describes the effective transmission behavior of the two-layer system.

The optimal distance obtained from the analytical solution is computed to be $d_r^{\mathrm{opt}} \approx 0.05538$; see Figure 4.2. In order to test the validity of our numerical method, we compare this value against the optimal distance, $d_{\mathrm{opt}} = 0.05245$, obtained by numerically computed

the energy transmission ratio; see Figure 3.4. Both values are in very good agreement. We attribute the small discrepancy of both values to the different current sources that were used.

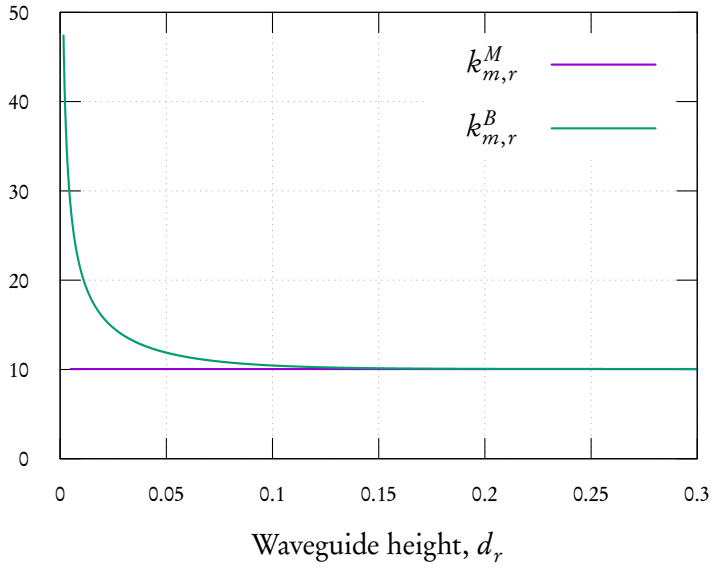

(a) Real part of the wavenumbers.

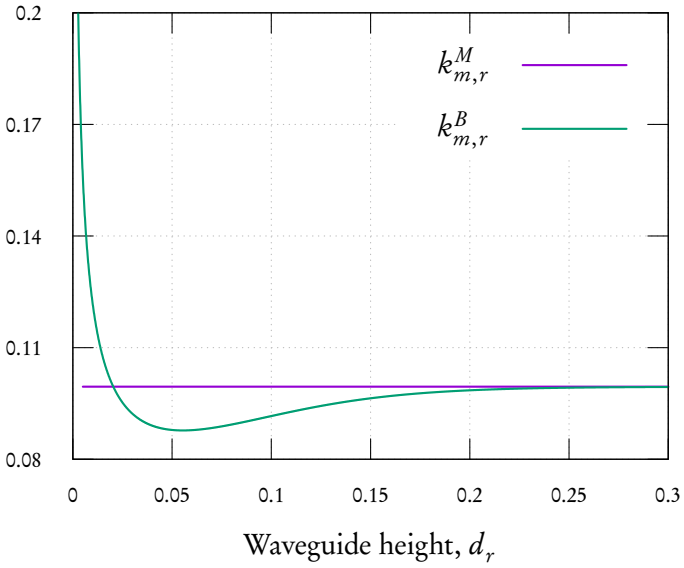

(b) Imaginary part of the wavenumbers.

Figure 4.2: Convergence of the two-layer system wavenumber $k^B_{m,r}$ to single-layer wavenumber $k^M_{m,r}$ numerically computed with a root solver for (4.15). The minimum loss is observed at $d_r = d_r^{\text{opt}} \approx 0.05538$.

Chapter 5

A class of nonlinear quartic eigenvalue problems arising in coupled Helmholtz equations

A conventional approach to analyzing waveguide problems is to first reduce Maxwell's equations to a Helmholtz eigenvalue problem. For a homogeneously filled waveguide, the EM fields decouple from one another, making the numerical simulation straightforward. However, if spatially dependent material parameters (gradient-index materials) are introduced, the field components are no longer independent from each other, and we are left with a coupled *nonlinear eigenvalue problem*.

Computational approaches for solving nonlinear eigenvalue problems have been studied in the literature [29, 30, 31, 32]. They typically require specialized solvers not readily available in finite element [75] and numerical linear algebra tookits [77, 78]. We pursue a different approach that allows to use existing linear algebra techniques. To that end, we investigate a general class of waveguide configurations that consist of spatially dependent material parameters and contain (arbitrarily shaped) interior conducting 2D material interfaces.

In light of this discussion, we show how to solve a variational, nonlinear quartic eigenvalue problem arising from a waveguiding problem with spatially dependent material parameters and interior conducting interfaces. The nonlinear quartic character of the eigenvalue problem stems from the fact that the spatially dependent material parameters cause a strong

coupling between the otherwise decoupled transverse magnetic (TM) and transverse electric (TE) modes (as would normally be the case for the Helmholtz equation). We solve the quartic eigenvalue problem numerically by transforming it to a spectrally equivalent linear system using a quadratification [48] approach. Additional numerical tools, such as the Möbius transform and a perfectly matched layer (PML) are employed to assist with solving the eigenvalue problem. We verify our numerical method against analytical solutions for prototypical geometries with internal conducting interfaces. As a practical example, we demonstrate how an improved quality factor (defined by the ratio of the real and the imaginary part of the computed eigenvalues) can be obtained (a) for a family of gradient-index host materials, and (b) by deformation of the geometry.

5.1 Derivation of pertinent equations

We introduce a variational formulation for a relevant eigenvalue problem prescribed with a gradient-index host material with (arbitrarily shaped) conducting interfaces in the context of a waveguide configuration. A convenient rescaling of the equations to dimensionless forms is used [52].

The source-free time-harmonic Maxwell's equations are given by

$$\begin{cases} \nabla \times \boldsymbol{E} &= i\omega\mu\boldsymbol{H}, \\ \nabla \times \boldsymbol{H} &= -i\omega\varepsilon\boldsymbol{E}. \end{cases} \tag{5.1}$$

Here, $\mu = \mu(x,y)$ and $\varepsilon = \varepsilon(x,y)$ are spatially dependent material parameters. In order to study *guided modes* we make the additional ansatz

$$\boldsymbol{\mathscr{F}} \sim e^{ik_z z},$$

and decompose the fields $\boldsymbol{\mathscr{F}} = \{\boldsymbol{E},\boldsymbol{H}\}$ and the gradient operator, ∇, into their longitudinal and transverse parts, whence we obtain

$$\boldsymbol{\mathscr{F}} = \boldsymbol{\mathscr{F}}_s + \hat{z}\mathscr{F}_z, \quad \nabla = \nabla_s + ik_z\hat{z},$$

where the subscript s denotes the transverse direction and $\hat{z}$ denotes the unit vector in the z-direction. Next we introduce a convenient rescaling of the system to dimensionless form by

setting the characteristic wavenumber of the ambient space to 1 [52]. The rescaling introduced in this section slightly differs from the one presented in Section 3.1.1.

$$x \to \breve{x} = k_0 x, \quad \nabla_s \to \breve{\nabla}_s = \frac{1}{k_0}\nabla_s, \quad k_z \to \breve{k}_z = \frac{k_z}{k_0},$$
$$\mu \to \mu_r = \frac{1}{\mu_0}\mu, \quad \varepsilon \to \varepsilon_r = \frac{1}{\varepsilon_0}\varepsilon, \quad \sigma^\Sigma \to \sigma_r^\Sigma = \sqrt{\frac{\mu_0}{\varepsilon_0}}\,\sigma^\Sigma$$
$$E \to \breve{E} = \frac{k_0^2}{\omega\mu_0}E, \quad H \to \breve{H} = k_0 H, \quad M_a \to \breve{M}_a = \frac{k_0}{\omega\mu_0}M_a.$$

To lighten the use of notation, we omit the breve sign in the remainder of this section. The rescaled (2.4) is

$$\begin{cases} -i\mu_r \boldsymbol{H}(\boldsymbol{x}) + \nabla \times \boldsymbol{E}(\boldsymbol{x}) = -\boldsymbol{M}_a(\boldsymbol{x}), \\ \nabla \cdot \big(\mu_r(\boldsymbol{x})\boldsymbol{H}(\boldsymbol{x})\big) = \frac{1}{i}\nabla \cdot \boldsymbol{M}_a(\boldsymbol{x}), \\ i\varepsilon_r(\boldsymbol{x})\boldsymbol{E}(\boldsymbol{x}) + \nabla \times \boldsymbol{H}(\boldsymbol{x}) = \boldsymbol{J}_a(\boldsymbol{x}), \\ \nabla \cdot \big(\varepsilon_r(\boldsymbol{x})\boldsymbol{E}(\boldsymbol{x})\big) = \frac{1}{i}\nabla \cdot \boldsymbol{J}_a(\boldsymbol{x}). \end{cases} \tag{5.2}$$

Applying the rescaling to (2.5) and rewriting into tangential and normal part leads to the following interface conditions:

$$\begin{cases} [\boldsymbol{H}_s]_\Sigma \cdot \tau = \left[\frac{i}{k_s^2}(k_z \partial_\tau H_z + \varepsilon_r \partial_\nu E_z)\right]_\Sigma = \sigma_r^\Sigma E_z, \\ \qquad\qquad [H_z]_\Sigma = -\sigma_r^\Sigma \boldsymbol{E}_s \cdot \tau, \\ [\mu_r \boldsymbol{H}_s]_\Sigma \cdot \nu = \left[\frac{i\mu_r}{k_s^2}(k_z \partial_\nu H_z - \varepsilon_r \partial_\tau E_z)\right]_\Sigma = 0, \\ [\boldsymbol{E}_s]_\Sigma \cdot \tau = \left[\frac{i}{k_s^2}(k_z \partial_\tau E_z - \mu_r \partial_\nu H_z)\right]_\Sigma = 0, \\ \qquad\qquad [E_z]_\Sigma = 0, \\ [\varepsilon_r \boldsymbol{E}_s]_\Sigma \cdot \nu = \left[\frac{i\varepsilon_r}{k_s^2}(k_z \partial_\nu E_z + \mu_r \partial_\tau H_z)\right]_\Sigma = \frac{1}{i}\nabla_s \cdot (\sigma_r^\Sigma \boldsymbol{E}_s), \end{cases} \tag{5.3}$$

where ∂_τ and ∂_ν denote the derivative in the tangential and the normal direction, respectively; $k_s(x,y)^2 = \mu_r(x,y)\,\varepsilon_r(x,y) - k_z^2$ is a function in the transverse direction. We make an additional assumption that $\boldsymbol{J}_a = \boldsymbol{M}_a \equiv 0$, and carry out in detail the derivation of our weak formulation (5.19). As a preliminary step, we explain how the longitudinal component of the guided mode is derived.

5.1.1 Longitudinal component

The transverse and the longitudinal components of the rescaled time-harmonic Maxwell's equations with $e^{ik_z z}$ dependence are

$$\begin{cases} i\mu_r \boldsymbol{H}_s = \nabla_s \times \hat{z} E_z + ik_z \hat{z} \times \boldsymbol{E}_s, \\ -i\varepsilon_r \boldsymbol{E}_s = \nabla_s \times \hat{z} H_z + ik_z \hat{z} \times \boldsymbol{H}_s, \end{cases} \tag{5.4}$$

$$\begin{cases} \nabla_s \times \boldsymbol{E}_s = i\mu_r \hat{z} H_z, \\ \nabla_s \times \boldsymbol{H}_s = -i\varepsilon_r \hat{z} E_z. \end{cases} \tag{5.5}$$

and the corresponding jump conditions at an interface Σ are

$$\begin{cases} \left[\boldsymbol{\nu} \times (\boldsymbol{H}_s + \hat{z} H_z)\right]_\Sigma = \sigma_r^\Sigma \left\{ \left(\boldsymbol{\nu} \times (\boldsymbol{E}_s + \hat{z} E_z)\right) \times \boldsymbol{\nu} \right\}_\Sigma, \\ \left[\boldsymbol{\nu} \cdot \mu_r (\boldsymbol{H}_s + \hat{z} H_z)\right]_\Sigma = \left[\boldsymbol{\nu} \times (\boldsymbol{E}_s + \hat{z} E_z)\right]_\Sigma = 0, \\ \left[\boldsymbol{\nu} \cdot \varepsilon_r (\boldsymbol{E}_s + \hat{z} E_z)\right]_\Sigma = \dfrac{1}{i} \nabla \cdot \left(\sigma_r^\Sigma \left(\boldsymbol{E}_s + \hat{z} E_z\right)\right), \end{cases} \tag{5.6}$$

where $\boldsymbol{\nu}$ is the normal vector at Σ. Equate each component of (5.6) to obtain

$$\begin{cases} [(\boldsymbol{H}_s \cdot \tau)\hat{z}]_\Sigma = \sigma_r^\Sigma \left\{ (-E_z \tau) \times \boldsymbol{\nu} \right\}_\Sigma = \sigma_r^\Sigma E_z \hat{z}\Big|_\Sigma, \\ [-H_z \tau]_\Sigma = \sigma_r^\Sigma \left\{ (\boldsymbol{E}_s \cdot \tau)\hat{z} \times \boldsymbol{\nu} \right\}_\Sigma = \sigma_r^\Sigma \Big(\boldsymbol{E}_s \cdot \tau\Big)\tau\Big|_\Sigma, \\ [\mu_r \boldsymbol{H}_s]_\Sigma \cdot \boldsymbol{\nu} = [\boldsymbol{E}_s]_\Sigma \cdot \tau = [E_z]_\Sigma = 0, \\ [\varepsilon_r \boldsymbol{E}_s]_\Sigma \cdot \boldsymbol{\nu} = \dfrac{1}{i} \nabla \cdot (\sigma_r^\Sigma \boldsymbol{E}) \end{cases} \tag{5.7}$$

Substitute one of (5.4) into the other to obtain

$$\begin{cases} k_s^2 \boldsymbol{E}_s = i(k_z \nabla_s E_z + \mu_r \nabla_s \times H_z), \\ k_s^2 \boldsymbol{H}_s = i(k_z \nabla_s H_z - \varepsilon_r \nabla_s \times E_z). \end{cases} \tag{5.8}$$

The second-order time-harmonic Maxwell's equations are

$$\begin{aligned} (\nabla_s + ik_z \hat{z}) \times (\mu_r^{-1} (\nabla_s + ik_z \hat{z}) \times \boldsymbol{E}) - \varepsilon_r \boldsymbol{E} = 0, \\ (\nabla_s + ik_z \hat{z}) \times (\varepsilon_r^{-1} (\nabla_s + ik_z \hat{z}) \times \boldsymbol{H}) - \mu_r \boldsymbol{H} = 0, \end{aligned} \tag{5.9}$$

Equate the z-component of (5.9) to obtain the z-component of the second-order Maxwell system:

$$\begin{cases} \nabla_s \times \left(\mu_r^{-1} \nabla_s \times \hat{z} E_z\right) + ik_z \nabla_s \times \left(\mu_r^{-1} \hat{z} \times \boldsymbol{E}_s\right) - \varepsilon_r E_z = 0, \\ \nabla_s \times \left(\varepsilon_r^{-1} \nabla_s \times \hat{z} H_z\right) + ik_z \nabla_s \times \left(\varepsilon_r^{-1} \hat{z} \times \boldsymbol{H}_s\right) + \mu_r H_z = 0. \end{cases} \tag{5.10}$$

5.2 Variational Statement

Let $\Omega \subset \mathbb{R}^n$, where $n = 2,3$, be a simply connected and bounded domain with Lipschitz-continous piecewise smooth boundary, $\partial\Omega$. Assume, in addition, that Σ is a Lipschitz-continuous, piecewise smooth hypersurface. Let ν and τ denote the outer normal and the tangential vector on Σ (see Figure 5.1). Some algebraic manipulation shows that $\nabla_s \times \left(\mu_r^{-1}\nabla_s \times \hat{z}E_z\right) = -\nabla_s\cdot\left(\mu_r^{-1}\nabla_s \hat{z}E_z\right)$ and $\nabla_s \times \left(\mu_r^{-1}\hat{z}\times \boldsymbol{E}_s\right) = \hat{z}\nabla_s\cdot\left(\mu_r^{-1}\boldsymbol{E}_s\right)$, which can be used, in conjunction with (5.8) and (5.10) to obtain:

$$\begin{cases} -\nabla_s\cdot\left(\dfrac{\varepsilon_r}{k_s^2}\nabla_s E_z\right) - k_z\nabla_s\cdot\left(\dfrac{1}{k_s^2}\nabla_s\times\hat{z}H_z\right) - \varepsilon_r E_z = 0, \\ -\nabla_s\cdot\left(\dfrac{\mu_r}{k_s^2}\nabla_s H_z\right) + k_z\nabla_s\cdot\left(\dfrac{1}{k_s^2}\nabla_s\times\hat{z}E_z\right) - \mu_r H_z = 0. \end{cases} \tag{5.11}$$

We observe that if the domain is homogeneously filled and isotropic, the curl terms vanish, yielding the familiar decoupled Helmholtz equation for E_z and H_z. Now assume that

$$[\varepsilon_r]_\Sigma = 0, \qquad [\mu_r]_\Sigma = 0. \tag{5.12}$$

We multiply (5.11) by k_s^4 and distribute it in a particular manner that eases the handling of the inhomogeneities.

$$\begin{cases} -k_s^4\left(\left(\nabla_s\dfrac{1}{k_s^2}\right)\cdot\left(\varepsilon_r\nabla_s E_z\right) + \dfrac{1}{k_s^2}\nabla_s\cdot\left(\varepsilon_r\nabla_s E_z\right)\right) \\ \qquad\qquad - k_z k_s^4\left(\left(\nabla_s\dfrac{1}{k_s^2}\right)\cdot\left(\nabla_s\times\hat{z}H_z\right)\right) - \varepsilon_r k_s^4 E_z = 0 \\ -k_s^4\left(\left(\nabla_s\dfrac{1}{k_s^2}\right)\cdot\left(\mu_r\nabla_s H_z\right) + \dfrac{1}{k_s^2}\nabla_s\cdot\left(\mu_r\nabla_s H_z\right)\right) \\ \qquad\qquad + k_z k_s^4\left(\left(\nabla_s\dfrac{1}{k_s^2}\right)\cdot\left(\nabla_s\times\hat{z}E_z\right)\right) - \mu_r k_s^4 H_z = 0. \end{cases} \tag{5.13}$$

Since $\nabla_s k_s^{-2} = -k_s^{-4}\nabla_s k_s^2$, some algebra shows that the expression in the first line of (5.13) is equivalent to

$$\begin{aligned} &-k_s^4\left(\left(\nabla_s\frac{1}{k_s^2}\right)\cdot\left(\varepsilon_r\nabla_s E_z\right) + \frac{1}{k_s^2}\nabla_s\cdot\left(\varepsilon_r\nabla_s E_z\right)\right) \\ &\quad = \nabla_s k_s^2\cdot\left(\varepsilon_r\nabla_s E_z\right) - k_s^2\nabla_s\cdot\left(\varepsilon_r\nabla_s E_z\right) \\ &\quad = \nabla_s\cdot\left(k_s^2\left(\varepsilon_r\nabla_s E_z\right)\right) - 2k_s^2\nabla_s\cdot\left(\varepsilon_r\nabla E_z\right). \end{aligned} \tag{5.14}$$

Additionally, we note that the curl terms in (5.13) can be written as

$$
\begin{aligned}
(5.15)\quad -k_z k_s^4 \left(\left(\nabla_s \frac{1}{k_s^2} \right) \cdot \left(\nabla_s \times \hat{z} H_z \right) + \frac{1}{k_s^2} \nabla_s \cdot (\nabla_s \times \hat{z} H_z) \right) \\
= k_z \nabla_s k_s^2 \cdot (\nabla_s \times \hat{z} H_z) - k_z k_s^2 \nabla_s \cdot (\nabla_s \times \hat{z} H_z) \\
= k_z \nabla_s \cdot \left(k_s^2 \left(\nabla_s \times \hat{z} H_z \right) \right) - 2 k_z k_s^2 \nabla_s \cdot (\nabla_s \times \hat{z} H_z).
\end{aligned}
$$

Even though the last term vanishes, we keep it, as it will be later utilized to express the interface contribution nicely.

We now test with smooth functions φ and ψ, and integrate by parts to arrive at

$$
\begin{aligned}
(5.16)\quad -(k_s^2 \varepsilon_r \nabla_s E_z, \nabla_s \varphi) + 2(\varepsilon_r \nabla_s E_z, \nabla_s (\overline{k}_s^2 \varphi)) - k_z (k_s^2 \nabla_s \times \hat{z} H_z, \nabla_s \varphi) \\
+ 2 k_z (\nabla_s \times \hat{z} H_z, \nabla_s (\overline{k}_s^2 \varphi)) - (\varepsilon_r k_s^4 E_z, \varphi) \\
-(k_s^2 \mu_r \nabla_s H_z, \nabla_s \psi) + 2(\mu_r \nabla_s H_z, \nabla_s (\overline{k}_s^2 \psi)) + k_z (k_s^2 \nabla_s \times \hat{z} E_z, \nabla_s \psi) \\
- 2 k_z (\nabla_s \times \hat{z} E_z, \nabla_s (\overline{k}_s^2 \psi)) - (\mu_r k_s^4 H_z, \psi) \\
+ \langle [k_s^2 \varepsilon_r \partial_\nu E_z + k_s^2 k_z \partial_\tau H_z]_\Sigma, \varphi \rangle_\Sigma + \langle [k_s^2 \mu_r \partial_\nu H_z - k_s^2 k_z \partial_\tau E_z]_\Sigma, \psi \rangle_\Sigma.
\end{aligned}
$$

Using (5.3), (5.12), and (5.8), the interface contributions simplify to

$$
\begin{aligned}
(5.17)\quad \langle [k_s^2 (\varepsilon_r \partial_\nu E_z + k_z \partial_\tau H_z)]_\Sigma, \varphi \rangle_\Sigma + \langle [k_s^2 (\mu_r \partial_\nu H_z - k_z \partial_\tau E_z)]_\Sigma, \psi \rangle_\Sigma \\
= -i \langle [k_s^4 \boldsymbol{H}_\tau]_\Sigma, \varphi \rangle_\Sigma - i \langle [k_s^4 \boldsymbol{E}_\tau]_\Sigma, \psi \rangle_\Sigma = -i \sigma_r^\Sigma \langle k_s^4 E_z, \varphi \rangle_\Sigma.
\end{aligned}
$$

Expand the $\nabla_s (\overline{k}_s^2 \varphi)$ and $\nabla_s (\overline{k}_s^2 \psi)$ to arrive at

$$
\begin{aligned}
(5.18)\quad (\mu_r \varepsilon_r{}^2 \nabla_s E_z, \nabla_s \varphi) + 2(\varepsilon_r \nabla_s E_z, \nabla_s (\overline{\varepsilon}_r \overline{\mu}_r) \varphi) \\
+ k_z (\mu_r \varepsilon_r \nabla_s \times \hat{z} H_z, \nabla_s \varphi) - k_z^2 (\varepsilon_r \nabla_s E_z, \nabla_s \varphi) \\
+ 2 k_z (\nabla_s \times \hat{z} H_z, \nabla_s (\overline{\varepsilon}_r \overline{\mu}_r) \varphi) - k_z^3 (\nabla_s \times \hat{z} H_z, \nabla_s \varphi) - (\varepsilon_r k_s^4 E_z, \varphi) \\
+ (\varepsilon_r \mu_r{}^2 \nabla_s H_z, \nabla_s \psi) + 2(\mu_r \nabla_s H_z, \nabla_s (\overline{\varepsilon}_r \overline{\mu}_r) \psi) \\
- k_z (\mu_r \varepsilon_r \nabla_s \times \hat{z} E_z, \nabla_s \psi) - k_z^2 (\mu_r \nabla_s H_z, \nabla_s \psi) \\
- 2 k_z (\nabla_s \times \hat{z} E_z, \nabla_s (\overline{\varepsilon}_r \overline{\mu}_r) \psi) + k_z^3 (\nabla_s \times \hat{z} E_z, \nabla_s \psi) - (\mu_r k_s^4 H_z, \psi) \\
- i \sigma_r^\Sigma \langle k_s^4 E_z, \varphi \rangle_\Sigma = 0.
\end{aligned}
$$

Proposition 5.2.1. *The nonlinear eigenvalue problem*

(N) *Find $k_z \in \mathbb{C}$ and E_z, H_z s. t.* (5.11) *and* (5.3) *are satisfied*

can be rewritten as a quartic eigenvalue problem

(Q) *Find $k_z \in \mathbb{C}$ and E_z, $H_z \in H^1(\Omega)$ s. t.*

$$\mathcal{Q}\big(k_z,(E_z,H_z)\big)\big[(\varphi,\psi)\big] = 0 \qquad \text{for all } \varphi,\ \psi \in H^1(\Omega),$$

where

$$\mathcal{Q}\big(k_z,(E_z,H_z)\big)\big[(\varphi,\psi)\big] = \sum_{l=0}^{4} (k_z)^l\, a_l\big((E_z,H_z)\big)\big[(\varphi,\psi)\big],$$

and

$$\begin{cases}
a_0((E_z,H_z),(\varphi,\psi)) = (\varepsilon_r^2 \nabla_s E_z, \nabla_s \varphi) + 2(\varepsilon_r \nabla_s E_z, (\nabla_s \overline{\varepsilon}_r)\varphi) \\
\qquad\qquad -(\varepsilon_r^3 E_z, \varphi) + (\varepsilon_r \nabla_s H_z, \nabla_s \psi) \\
\qquad\qquad +2(\nabla_s H_z, (\nabla_s \overline{\varepsilon}_r)\psi) - (\varepsilon_r^2 H_z, \psi) \\
\qquad\qquad -i\langle \sigma_r^{\Sigma} \varepsilon_r^2 E_z, \varphi\rangle_{\Sigma}, \\
a_1((E_z,H_z),(\varphi,\psi)) = (\varepsilon_r \nabla_s \times \hat{z} H_z, \nabla_s \varphi) \\
\qquad\qquad +2(\nabla_s \times \hat{z} H_z, (\nabla_s \overline{\varepsilon}_r)\varphi) \\
\qquad\qquad -(\varepsilon_r \nabla_s \times \hat{z} E_z, \nabla_s \psi) \\
\qquad\qquad -2(\nabla_s \times \hat{z} E_z, (\nabla_s \overline{\varepsilon}_r)\psi) \\
a_2((E_z,H_z),(\varphi,\psi)) = -(\varepsilon_r \nabla_s E_z, \nabla_s \varphi) + 2(\varepsilon_r^2 E_z, \varphi) \\
\qquad\qquad -(\nabla_s H_z, \nabla_s \psi) + 2(\varepsilon_r H_z, \psi) \\
\qquad\qquad +2i\langle \sigma_r^{\Sigma} \varepsilon_r E_z, \varphi\rangle_{\Sigma}, \\
a_3((E_z,H_z),(\varphi,\psi)) = -(\nabla_s \times \hat{z} H_z, \nabla_s \varphi) + (\nabla_s \times \hat{z} E_z, \nabla_s \psi), \\
a_4((E_z,H_z),(\varphi,\psi)) = -(\varepsilon_r E_z, \varphi) - (H_z, \psi) - i\langle \sigma_r^{\Sigma} E_z, \varphi\rangle_{\Sigma}.
\end{cases} \tag{5.19}$$

5.3 Numerical approach

In this section, we outline our numerical approach for solving the quartic eigenvalue problem (Q). In particular we discuss a *quadratification* approach transforming the quartic eigenvalue problem into a larger, linear eigenvalue problem with equivalent spectrum. A perfectly matched layer (PML), an artificial sponge layer placed near the boundary such that all outgoing waves decay exponentially, is introduced. The variational formulation (Q) is discretized on a non-uniform quadrilateral mesh.

Proposition 5.3.1. *Let $X_h(\Omega) \subset X(\Omega)$ be a finite element subspace spanned by Lagrange finite elements Q_p.*

$$(\mathrm{Q}_h) \qquad \sum_{l=0}^{4} k_z^l a_l((E_z, H_z), (\varphi, \psi)) = 0,$$

Our goal is to translate (Q_h) into a finite dimensional linear problem, which then allows the use of a standard linear algebra solver.

5.3.1 Quadratification of the Quartic Eigenvalue Problem

We build upon the algebraic tool of *quadratification* introduced in [48], which allows us to reduce any even power matrix polynomial eigenvalue problem to a spectrally equivalent linear eigenvalue problem. Prop. 5.3.2 summarizes the main result (for a more general discussion of the ideas behind this reduction procedure, we refer the reader to [48]).

Proposition 5.3.2 (Theorem 5.3 and 5.4 of [48])**.** *Consider a quartic eigenvalue problem, to find $\lambda \in \mathbb{C}$, and $x \in \mathbb{C}^n$, s. t.*

$$\sum_{k=0}^{4} \lambda^k A_k x = 0,$$

where $A_k \in \mathbb{C}^{n \times n}$ are given matrices. Then, the linearization *stated below is spectrally equivalent to the original problem (c.f. [48] Theorem 5.3 and 5.4): Find $\lambda \in \mathbb{C}$, and $z \in \mathbb{C}^{4n}$ s. t.*

$$\begin{pmatrix} A_3 & 0 & -I_n & 0 \\ A_1 & 0 & 0 & -I_n \\ 0 & -I_n & 0 & 0 \\ A_0 & 0 & 0 & 0 \end{pmatrix} z + \lambda \begin{pmatrix} A_4 & 0 & 0 & 0 \\ A_2 & I_n & 0 & 0 \\ 0 & 0 & I_n & 0 \\ 0 & 0 & 0 & I_n \end{pmatrix} z = 0. \tag{5.20}$$

Here, I_n denotes the $n \times n$ identity matrix.

With this result at hand, we rewrite (Q_h) as a linear eigenvalue problem:

$$(\mathrm{LQ}_h) \qquad S z + \lambda M z = 0,$$

where

$$S = \begin{pmatrix} a_3 & 0 & -I_n & 0 \\ a_1 & 0 & 0 & -I_n \\ 0 & -I_n & 0 & 0 \\ a_0 & 0 & 0 & 0 \end{pmatrix}, \quad M = \begin{pmatrix} a_4 & 0 & 0 & 0 \\ a_2 & I & 0 & 0 \\ 0 & 0 & I & 0 \\ 0 & 0 & 0 & I \end{pmatrix}, \quad z = \begin{pmatrix} z_1 \\ z_2 \\ z_3 \\ z_4 \end{pmatrix}.$$

Here, by some abuse of notation a_i denotes the corresponding matrix formed by the bilinear form $a_i(..)$ given in (5.19) and by fixing a basis of $X_h(\Omega)$. A quick computation shows that the eigenvectors of the original problem (Q_h) and of the final linearized problem (LQ_h) are related as follows.

Proposition 5.3.3. *Let $\lambda \in \mathbb{C}$ and $x \in \mathbb{C}^n$ be an eigenvalue with corresponding eigenvector of (Q_h). Then, λ and $z \in \mathbb{C}^{4n}$ given by*

$$\begin{cases} z_1 &= \lambda x, \\ z_2 &= \lambda^2(a_3 + \lambda a_4)x, \\ z_3 &= \lambda(a_3 + \lambda a_4)x, \\ z_4 &= -a_0 x, \end{cases} \tag{5.21}$$

is an eigenvalue with corresponding eigenvector of (LQ_h). Conversely, if $\lambda \in \mathbb{C}$ and $z \in \mathbb{C}^{4n}$ is an eigenvalue and eigenvector pair of (LQ_h), then provided that $\det(a_0) \neq 0$ and $\det(\lambda a_4 + a_3) \neq 0$, the vector z is characterized by (5.21) and λ and x are an eigenvalue and eigenvector pair of (Q_h).

5.3.2 Perfectly Matched Layer

A perfectly matched layer (PML) is a truncation procedure motivated from electromagnetic scattering problems in the time domain. The idea is to surround the computational domain with a so-called sponge layer, an artificial boundary wherein all outgoing electromagnetic waves decay exponentially with minimal artificial reflection. As outlined in [79, 49, 52], we

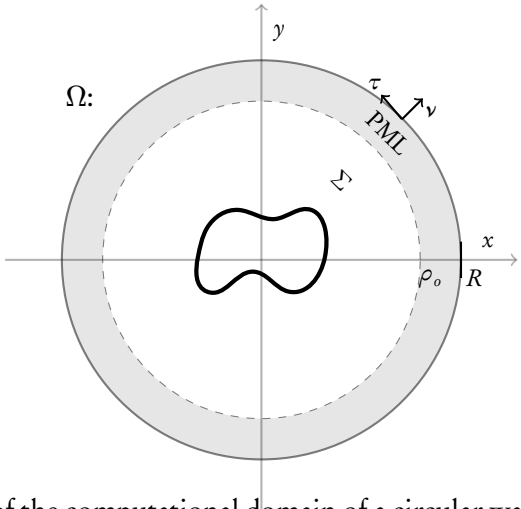

Figure 5.1: Schematic of the computational domain of a circular waveguide Ω, with boundary $\partial\Omega$, outer normal vector ν, and tangential vector τ. A conducting ciruclar interface is labeled Σ. A perfectly matched layer (PML) is enforced in the shaded region.

carry out a change of coordinates from the computational domain with real-valued coordinates to a domain with complex-valued coordinates. We refer the reader to [79] for details. For a spherical absorption layer, we define the transformation $\tilde{\rho} = \rho\overline{d}$, where

$$d = 1 + is(r), \quad \overline{d} = 1 + i/r \int_{\rho}^{r} s(\tau)\, d\tau,$$

and $s(\tau)$ is an appropriately chosen, nonnegative scaling function. Applying the above transformation, the quartic eigenvalue problem takes the following rescaled form within the PML:

$$\begin{aligned}
&\hat{\nabla}_s \cdot (k_s^2(\varepsilon_r \hat{\nabla}_s \hat{E}_z)) - 2k_s^2 \hat{\nabla}_s \cdot (\varepsilon_r \hat{\nabla}_s \hat{E}_z) + k_z \hat{\nabla}_s \cdot (k_s^2 \hat{\nabla}_s \times \hat{H}_z) \\
&\qquad - 2k_z k_s^2 \hat{\nabla}_s \cdot (\hat{\nabla}_s \times \hat{H}_z) + \hat{\nabla}_s \cdot (k_s^2(\mu_r \hat{\nabla}_s \hat{H}_z)) - 2k_s^2 \hat{\nabla}_s \cdot (\mu_r \hat{\nabla}_s \hat{H}_z) \\
&\qquad\qquad + k_z \hat{\nabla}_s \cdot (k_s^2 \hat{\nabla}_s \times \hat{E}_z) + 2k_z k_s^2 \hat{\nabla}_s \cdot (\hat{\nabla}_s \times \hat{E}_z) \\
&\qquad\qquad\qquad - \varepsilon_r k_s^4 \hat{E}_z - \mu_r k_s^4 \hat{H}_z = 0.
\end{aligned}$$

This can be rewritten as

$$\begin{aligned}\frac{1}{d\overline{d}}\nabla_s\cdot(k_s^2\varepsilon_r A\nabla_s E_z)-\frac{2k_s^2}{d\overline{d}}\nabla_s\cdot(\varepsilon_r A\nabla_s E_z)+\frac{k_z}{d\overline{d}}\nabla_s\cdot(k_s^2\nabla_s\times H_z)\\ -\frac{2k_zk_s^2}{d\overline{d}}\nabla_s\cdot(\nabla_s\times H_z)+\frac{1}{d\overline{d}}\nabla_s\cdot(k_s^2\varepsilon_r A\nabla_s E_z)-\frac{2k_s^2}{d\overline{d}}\nabla_s\cdot(\varepsilon_r A\nabla_s E_z)\\ +\frac{k_z}{d\overline{d}}\nabla_s\cdot(k_s^2\nabla_s\times H_z)+\frac{2k_zk_s^2}{d\overline{d}}\nabla_s\cdot(\nabla_s\times E_z)\\ +\varepsilon_r k_s^4E_z+\mu_r k_s^4H_z=0,\end{aligned}$$

where $A=T^{-1}_{\boldsymbol{e}_x,\boldsymbol{e}_r}\operatorname{diag}(\overline{d}/d,d/\overline{d})T_{\boldsymbol{e}_x,\boldsymbol{e}_r}$, and $T_{\boldsymbol{e}_x,\boldsymbol{e}_r}$ is the rotation matrix that rotates $\boldsymbol{e}_r$ onto $\boldsymbol{e}_x$. We enforce the condition that the material parameters are constant outside the PML, i.e., ε_r and μ_r do not undergo a change of coordinate. Additionally, because the eigenmodes of our interest are confined to the conducting interface, which is situated inside the PML, no coordinate change is needed for the jump condition. The modified bilinear forms, $\tilde{a}_i$, are

$$\begin{cases}\tilde{a}_0((E_z,H_z),(\varphi,\psi))=(\varepsilon_r^2A\nabla_sE_z,\nabla_s\varphi)+2(\varepsilon_rA\nabla_sE_z,(\nabla_s\overline{\varepsilon}_r)\varphi)\\ \qquad -d\overline{d}\,(\varepsilon_r^3E_z,\varphi)+(\varepsilon_rA\nabla_sH_z,\nabla_s\psi)\\ \qquad +2(A\nabla_sH_z,(\nabla_s\overline{\varepsilon}_r)\psi)-d\overline{d}\,(\varepsilon_r^2H_z,\psi)\\ \qquad -i\langle\sigma_r^{\Sigma}\varepsilon_r^2E_z,\varphi\rangle_{\Sigma},\\ \tilde{a}_1((E_z,H_z),(\varphi,\psi))=(\varepsilon_r\nabla_s\times\hat{z}H_z,\nabla_s\varphi)\\ \qquad +2(\nabla_s\times\hat{z}H_z,(\nabla_s\overline{\varepsilon}_r)\varphi)\\ \qquad -(\varepsilon_r\nabla_s\times\hat{z}E_z,\nabla_s\psi)\\ \qquad -2(\nabla_s\times\hat{z}E_z,(\nabla_s\overline{\varepsilon}_r)\psi)\\ \tilde{a}_2((E_z,H_z),(\varphi,\psi))=-(\varepsilon_rA\nabla_sE_z,\nabla_s\varphi)+2d\overline{d}\,(\varepsilon_r^2E_z,\varphi)\\ \qquad -(A\nabla_sH_z,\nabla_s\psi)+2d\overline{d}\,(\varepsilon_rH_z,\psi)\\ \qquad +2i\langle\sigma_r^{\Sigma}\varepsilon_rE_z,\varphi\rangle_{\Sigma},\\ \tilde{a}_3((E_z,H_z),(\varphi,\psi))=-(\nabla_s\times\hat{z}H_z,\nabla_s\varphi)+(\nabla_s\times\hat{z}E_z,\nabla_s\psi),\\ \tilde{a}_4((E_z,H_z),(\varphi,\psi))=-d\overline{d}\,(\varepsilon_rE_z,\varphi)-d\overline{d}\,(H_z,\psi)-i\langle\sigma_r^{\Sigma}E_z,\varphi\rangle_{\Sigma}.\end{cases}\tag{5.22}$$

5.3.3 Möbius Transform

The Möbius transformation is an efficient tool that transforms the given eigenvalue problem into a related one, for which eigenvalues of interest in the transformed spectrum are close to 0 (or maximal), so that they can be selectively computed with conventional Krylov-space iteration techniques. It is a conformal mapping, defined as follows.

$$\lambda \mapsto \frac{a\lambda + b}{c\lambda + d},$$

where $\lambda, a, b, c, d \in \mathbb{C}$. Over arbitrary fields, the Möbius transformation preserves a number of spectral features of matrix polynomials, such as regularity, rank, minimal indicies, the location of zero entries, symmetry, and skew-symmetry [80]. In particular, every Möbius transformation preserves the relation of spectral equivalence [80]. The computational eigenvalue problem, after introducing a PML, truncating the domain, and applying finite elements, can be written as

$$Sz = k_z M z, \tag{5.23}$$

for a complex-valued vector z and appropriate complex-valued matrices S and M. The implementation of the PML discussed in 5.3.2 necessitates changes to the definition of a_1, a_2, a_3, and a_4. The idea is to use the Möbius transform to map points near the origin to target values

$$(aS + bM)z = \tilde{k}_z(cS + dM)z, \tag{5.24}$$

where a, b, c, d are the Möbius transform parameters. The original eigenvalue can be retrieved via the inverse Möbius transform $k_z = (-b + d\tilde{k}_z)/(a - c\tilde{k}_z)$.

5.4 Validation of weak formulation

In this section, the analytical solution for constant material parameters is derived and discussed. We use the analytic result to validate our numerical approach.

By assuming constant material parameters, the quartic eigenvalue problem (Q) does not exhibit any hybridization and reduces to a linear eigenvalue problem: Find $u \in H^1(\Omega, \mathbb{C})$ s. t.

$$\mathscr{L}(u)[\varphi] := a(u, \varphi) + k_z^2\, m(u, \varphi), \tag{L}$$

	Eigenvalues from (L)	Eigenvalues from (Q)	Eigenvalues from (5.28)
Mode	k_z	k_z	k_z
1	$9.447 \pm 0.090468i$	$9.447 \pm 0.090467i$	$9.447 \pm 0.090467i$
2	$13.00 \pm 0.090641i$	$13.00 \pm 0.090640i$	$13.00 \pm 0.090641i$
3	$16.17 \pm 0.099812i$	$16.17 \pm 0.099812i$	$16.17 \pm 0.099813i$

Table 5.1: Validation of computed eigenvalues form the linear problem (5.25), the quartic problem (Q), and the analytical approach (5.28) for a single-layer waveguide. Note that the values obtained are in agreement with confidence level of less than 1%. Parameters used are $R = 2.0, \sigma_r^\Sigma = 0.002 + 0.20i, \varepsilon_r = \mu_r \equiv 1$, and $\rho_i = 0.3$.

for $\varphi \in H^1(\Omega, \mathbb{C})$ and where we have introduced the bilinear forms

$$\begin{cases} a(u,\varphi) = \int_\Omega \nabla_s u \cdot \nabla_s \overline{\varphi}\, \mathrm{d}x - \int_\Omega \mu_r\, \varepsilon_r\, u\, \overline{\varphi}\, \mathrm{d}x - i \int_\Sigma \mu_r\, \sigma_r^\Sigma u\, \overline{\varphi}\, \mathrm{d}o_x, \\ m(u,\varphi) = \int_\Omega u\, \overline{\varphi}\, \mathrm{d}x + i \int_\Sigma \sigma_r^\Sigma \varepsilon_r^{-1}\, u\, \overline{\varphi}\, \mathrm{d}o_x. \end{cases} \tag{5.25}$$

For a simple spherical geometry that is rotationally invariant, the field solution can be expressed as a superposition of the modified Bessel functions of the first and second kind. In the case of a waveguide with a single circular interface Σ, i.e., where Σ is described by a circle with origin 0 and radius R, the analytical solution takes the following form.

$$E_z = \begin{cases} A_m I_m(ik_s\rho) e^{im\theta} e^{ik_z z} & \text{for } \rho < R, \\ B_m K_m(ik_s\rho) e^{im\theta} e^{ik_z z} & \text{for } \rho > R, \end{cases} \tag{5.26}$$

$$H_z = \begin{cases} C_m I_m(ik_s\rho) e^{im\theta} e^{ik_z z} & \text{for } \rho < R, \\ D_m K_m(ik_s\rho) e^{im\theta} e^{ik_z z} & \text{for } \rho > R, \end{cases} \tag{5.27}$$

where I_m and K_m denote the modified Bessel functions of the first and second kind, respectively, and A_m, B_m, C_m, and D_m are constants that are determined by the boundary conditions [13, 8]. Assuming that the conducting film is located on the boundary of the interior circle with radius R, we equate the jump conditions (5.3) of each field component. Then (5.3) reduces to the following algebraic condition, from which we can retrieve the propagation constant, k_z:

$$\det(M - \sigma_r^\Sigma N) = 0, \tag{5.28}$$

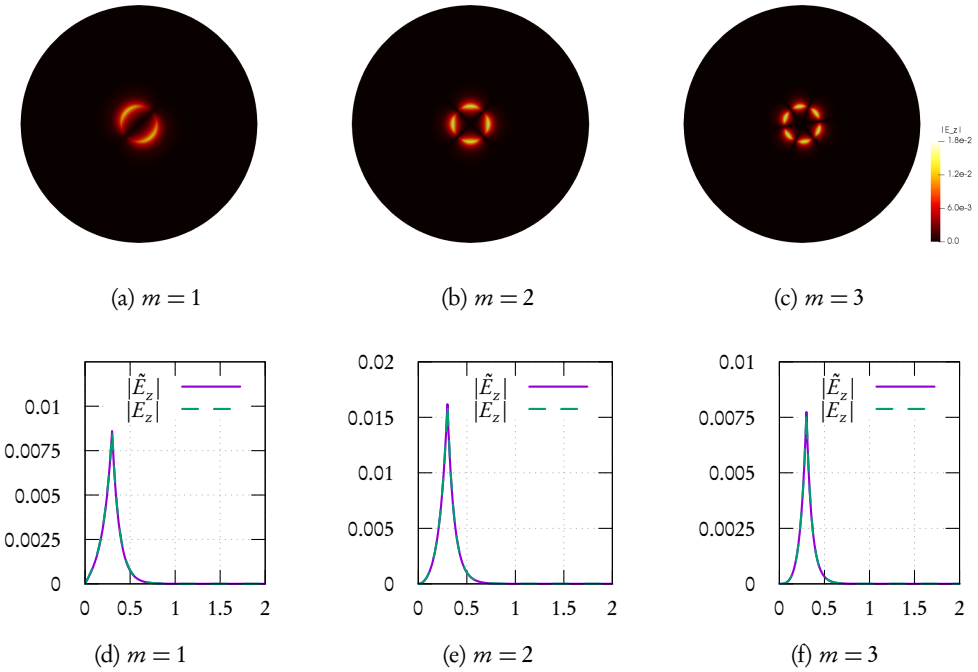

(a) $m = 1$ (b) $m = 2$ (c) $m = 3$

(d) $m = 1$ (e) $m = 2$ (f) $m = 3$

Figure 5.2: Computational results for modal order $m = 1, 2, 3$ for a spherical reference configuration with constant material parameters, with interior radius $\rho_i = 0.3$, $\sigma_r^{\Sigma} = 0.002 + 0.20i$, and $R = 2.0$. (a-c) shows the magnitude of the numerically computed electric field, $\tilde{E}_z$. The computed electric field is compared against an analytic solution, E_z, in (d)-(f).

where

$$M := \begin{pmatrix} I_m(ik_sR) & 0 & -K_m(ik_sR) & 0 \\ \frac{k_z m I_m(ik_sR)}{Rk_s^2} & -\frac{\mu I'_m(ik_sR)}{k_s} & -\frac{k_z m K_m(ik_sR)}{Rk_s^2} & \frac{\mu K'_m(ik_sR)}{k_s} \\ \frac{\epsilon_1 I'_m(ik_sR)}{k_s} & \frac{k_z m I_m(ik_sR)}{Rk_s^2} & -\frac{\epsilon_2 K'_m(ik_sR)}{k_s} & -\frac{k_z m K_m(ik_sR)}{Rk_s^2} \\ 0 & I_m(ik_sR) & 0 & -K_m(ik_sR) \end{pmatrix}$$

and

$$N := \begin{pmatrix} 0 & 0 & 0 & 0 \\ 0 & 0 & 0 & 0 \\ I_m(ik_sR) & 0 & 0 & 0 \\ -\frac{k_z m I_m(ik_sR)}{Rk_s^2} & \frac{\mu I'_m(ik_sR)}{k_s} & 0 & 0 \end{pmatrix}.$$

We numerically solve the zeroes of the determinant of the difference of the above matrices via a root finding algorithm for modal orders $m = 1, 2$ and 3. The computed values are then compared against those of the linear problem (L) and of the quartic problem (Q) (see Table 5.1 and Figure 5.2).

We now validate our numerics with the analytical results. Three validations are carried out: analytical, numerical with linear eigenvalue, and lastly, the quartic eigenvalue problem. For simplicity, we assume the computational domain is isotropic, with material parameters $\varepsilon_r = \mu_r \equiv 1$. A conducting interface is coated on the boundary of the interior circle with radius $\rho_i = 0.3$, and choose $R = 2.0$. The surface conductivity is set to $\sigma_r^{\Sigma} = 0.002 + 0.20i$.

The analytic computation of the propagation constant k_z requires finding the complex roots of the determinant of the 4×4 matrix. We will consider modal orders of $m = 1, 2$ and 3 to ease the computation. The computational results displayed in Table 5.1 deviate by less than 1% from each other. We can thus expect a confidence level of 1% or better in our numerical computations. Figure 5.2 shows the intensity of the numerically computed electric field,$||E_z||_2$, and a comparison of, both, the analytic and numerical solutions. We thus conclude that our numerical framework is a reliable model that can effectively simulate hybrid plasmonic modes.

5.5 Numerical results for a spherical geometry with circular and arbitrary interface

These eigenvalues are numerically computed using SLEPc [78], a general purpose eigensolver built on top of PETSc [77]. The eigensolver provides a number of Krylov-space methods, such as the Arnoldi, Lanczos, Krylov-Schur, and conjugate-gradient methods. For our purposes, we will make use of the Krylov-Schur method for its faster convergence.

In this section, we present a number of computational results obtained from solving the quartic eigenvalue problem (Q). We examine numerically how the spectrum of a hybridized configuration behaves under modification of spatially dependent material parameters, $\varepsilon_r(\rho,\theta)$. We further investigate the relationship between mesh deformation and a quality factor, and study the degree by which the spectrum changes. All numerical computations are carried out with the finite element library deal.II [74, 75]. We use a Krylov-Schur method to compute solutions of the linearized eigenproblem (LQ_h) [78].

We demonstrate numerically how it is possible to attain an improved quality factor by prescribing the host material with a radially-varying refractive index profile. This is methodically carried out in the subsequent subsections. First, a parameter study is conducted to validate our choice of discretization parameters. Second, we solve the quartic eigenvalue problem (LQ_h) using a number of permittivity functions, and observe how the spectrums differ from those obtained in an isotropic medium. Lastly, we deform our computational domain to demonstrate that our numerical framework is equipped to handle even the most general configuration. The key idea behind this generalization is to show that we can manipulate the spectrum by manipulating the shape. We make note of the evolution of eigenmodes, and how our framework can be used as a basis for shape optimization of gradient-index waveguides.

5.5.1 Validation of discretization parameters

The computational domain, Ω, is chosen to be the circle with radius 1. A spherical PML is enforced for $\rho > 0.8$. The surface conductivity $\sigma_r^{\Sigma} = 0.002 + 0.20i$ is chosen that is within a realistic parameter range [52]. Following [49], the nonnegative scaling function $s(\rho)$ is chosen to be

$$s(\rho) = s_0 \frac{(\rho - 0.8R)^2}{(R - 0.8R)^2}, \tag{5.29}$$

where we set the free parameter s_0 to be $s_0 = 1.5$ in our computations. We carry out a parameter study to test the validity and the sensitivity of discretization parameters. Table 5.2 summarizes the parameter study quantitatively. As can be seen, the eigenmodes comptued are stable with respect to variations of PML strength s_0, the number of initial refinements k, and domain sizes R. A spectral transformation is carried out in the form of the Möbius transformation, with the parameters chosen to be $a = 1, b = -10, c = 1, d = 10$. We conclude that $R = 1.0$ and $k = 5$ is a valid choice of discretization parameters.

	$s_o = 1.5, R = 1.0, k = 4, \text{DoF} = 19138$			$s_o = 1.5, R = 1.0, k = 6, \text{DoF} = 303874$		
Mode	$\text{Re}k_z$	$\text{Im}k_z$	$\text{Re}k_z/\text{Im}k_z$	$\text{Re}k_z$	$\text{Im}k_z$	$\text{Re}k_z/\text{Im}k_z$
0	17.4869	0.13035	134.153	17.1839	0.12764	134.628
1	30.5400	0.17646	173.070	30.4160	0.17540	173.409
2	40.5520	0.21898	185.186	40.5043	0.21881	185.112
3	48.8115	0.25681	190.069	48.7719	0.25662	190.055
4	55.9587	0.29058	192.576	55.8971	0.29026	192.576
5	62.3394	0.32120	194.083	62.2388	0.32068	194.084

(a) Vary the number of refinements, k.

	$s_o = 1.5, R = 1.0, k = 5, \text{DoF} = 76162$		
Mode	$\text{Re}k_z$	$\text{Im}k_z$	$\text{Re}k_z/\text{Im}k_z$
0	17.1839	0.12764	134.628
1	30.4160	0.17582	172.995
2	40.5043	0.21881	185.112
3	48.7719	0.25662	190.055
4	55.8971	0.29025	192.583
5	62.2388	0.32068	194.084

(b) The control case for the parameter studies.

	$s_o = 1.5, R = 0.5, k = 5, \text{DoF} = 76162$			$s_o = 1.5, R = 2.0, k = 5, \text{DoF} = 76162$		
Mode	$\text{Re}k_z$	$\text{Im}k_z$	$\text{Re}k_z/\text{Im}k_z$	$\text{Re}k_z$	$\text{Im}k_z$	$\text{Re}k_z/\text{Im}k_z$
0	17.0933	0.12676	134.848	171.839	0.12764	134.628
1	30.4242	0.17528	173.575	30.8567	0.17331	178.043
2	40.4905	0.21876	185.091	40.5043	0.21881	185.112
3	48.7682	0.25661	190.048	48.7719	0.25662	190.055
4	55.8962	0.29026	192.573	55.8971	0.29026	192.576
5	62.2387	0.32068	194.084	62.2389	0.32068	194.084

(c) Vary the domain size, R.

Table 5.2: Parameter study with permittivity function $\varepsilon_r(\boldsymbol{x}) = 3 \cdot \chi_{|\boldsymbol{x}|<\rho_i} + 1 \cdot \chi_{\rho_i<|\boldsymbol{x}|<R}$. $\mu_r(\boldsymbol{x}) \equiv 1$ and $\sigma_r^{\Sigma} = 0.002 + 0.20i$. (b) is the control discretization parameters. (a) differs from (b) in the number of refinements, and (c) differs from (b) in the size of the domain.

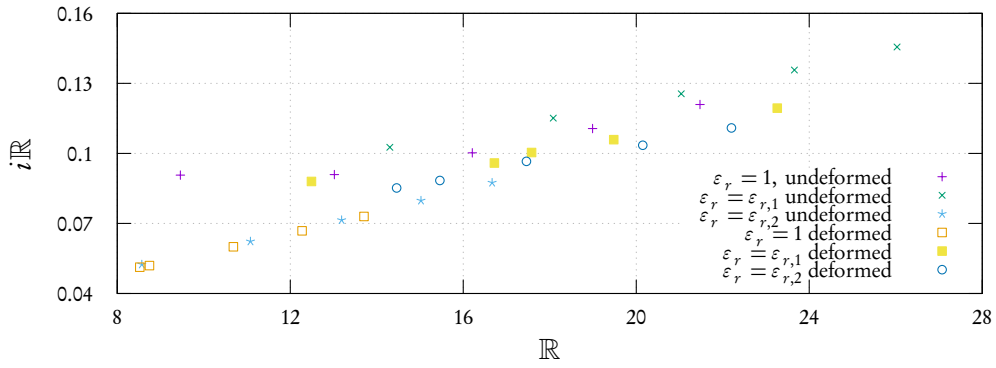

Figure 5.3: Spectrums computed using different ε_r for spherical and deformed domain. For $\varepsilon_r \equiv 1$ and $\varepsilon_{r,1}$, both the real and the imaginary parts have decreased after the domain was deformed. The opposite is observed for $\varepsilon_{r,2}$. In the spherical domain case, the eigenvalues for $\varepsilon_r \equiv 1$ and $\varepsilon_{r,1}$ remain relatively close to one another, but undergo a noticeable difference after the mesh deformation. The opposite can be seen for $\varepsilon_{r,1}$ and $\varepsilon_{r,2}$.

5.5.2 Gradient-index waveguide

Our numerical framework admits any (locally) differentiable material parameters. To demonstrate this, we consider the following material permittivity functions and analyze their spectrums in relation to those of the isotropic medium.

$$\begin{cases} \varepsilon_{r,1}(\rho,\theta) = 1.2 + \dfrac{1}{2}\sin\left(\dfrac{\rho^2}{(2\rho_i)^2}\sin 2\theta\right)\exp\left(-\dfrac{(\rho-2\rho_i)^2}{(2\rho_i)^2}\right), \\ \varepsilon_{r,2}(\rho) = 1 + \left(\dfrac{\rho}{2} + \rho^2\sin\left(\dfrac{2\pi}{\rho}\right)\right)\exp\left(-\dfrac{(\rho-2\rho_i)^2}{2\rho_i}\right), \end{cases} \tag{5.30}$$

where ρ_o is the PML cutoff radius and ρ_i is the radius at which the conducting interface is situated for a circular waveguide. We set $\rho_o = 0.8$ and $\rho_i = 0.1$ for our computations. The key aspect of these functions is that ε_r remains constant in the PML, which enables us to implement the PML as laid out in 5.3.2. The computations are carried out using the unit circular waveguide. For comparison, we plot the eigenvalues for both isotropic media and materials defined by (5.30) (see Figure 5.3). The quality factor of the first 5 modes of each of these functions are laid out in Table 5.3. We make note of a few observations.

- The eigenvalues obtained from $\varepsilon_{r,i}$ are more clustered than those from isotropic media.

	$\varepsilon_r \equiv 1$			$\varepsilon_r = \varepsilon_{r,1}$			$\varepsilon_r = \varepsilon_{r,2}$		
Mode	$\mathrm{Re}k_z$	$\mathrm{Im}k_z$	η_3	$\mathrm{Re}k_z$	$\mathrm{Im}k_z$	η	$\mathrm{Re}k_z$	$\mathrm{Im}k_z$	η
1	13.02	0.09093	143.2	14.30	0.1026	139.4	8.569	0.05243	163.4
2	16.21	0.1003	161.7	18.08	0.1151	157.1	11.08	0.06230	177.9
3	18.99	0.1107	171.6	21.04	0.1256	167.6	13.19	0.07144	184.6
4	21.47	0.1210	177.6	23.66	0.1357	174.3	15.02	0.07979	188.3
5	23.74	0.1309	181.4	26.03	0.1456	178.8	16.67	0.08746	190.6

(a) Eigenvalues for spherical domain

	$\varepsilon_r \equiv 1$			$\varepsilon_r = \varepsilon_{r,1}$			$\varepsilon_r = \varepsilon_{r,2}$		
Mode	$\mathrm{Re}k_z$	$\mathrm{Im}k_z$	η_3	$\mathrm{Re}k_z$	$\mathrm{Im}k_z$	η	$\mathrm{Re}k_z$	$\mathrm{Im}k_z$	η
1	8.521	0.05126	166.2	12.49	0.0880	141.9	14.46	0.0852	169.8
2	8.745	0.05194	168.8	16.72	0.0959	163.8	15.46	0.0884	174.9
3	10.69	0.06003	178.0	17.58	0.1004	175.1	17.46	0.0966	182.1
4	12.27	0.06683	183.7	19.48	0.1059	184.0	20.15	0.1035	194.8
5	13.71	0.07300	187.8	23.26	0.1194	194.8	22.20	0.1109	200.2

(b) Eigenvalues for deformed domain

Table 5.3: Eigenvalues k_z and quality factor η for different ε_r in spherical and deformed domains. Noticeable shift in the spectrums is observed from (a) to (b), which in turn, has led to non-negligible increases in η.

Even though the range of $\varepsilon_{r,i}$ ($\varepsilon_{r,1} \in (1.0, 1.4)$ and $\varepsilon_{r,2} \in (1.0, 1.1614)$) is relatively close to 1, we observe significant changes to the spectrum and the quality factor.

- From Table 5.3, a much longer propagation is observed for $\varepsilon_{r,2}$ than for $\varepsilon_{r,1}$, despite their relatively similar range.

- This demonstrates that the relationship between ε_r and η is not trivial, and that it is possible to optimize η with a nontrivial ε_r.

5.5.3 Generalized configuration

Now, as a small study, we compute using the permittivity functions introduced in the preceding section, but in a deformed configuration, and demonstrate that we can use this generalization in the context for shape optimization. Meshes near the conducting interface are heavily

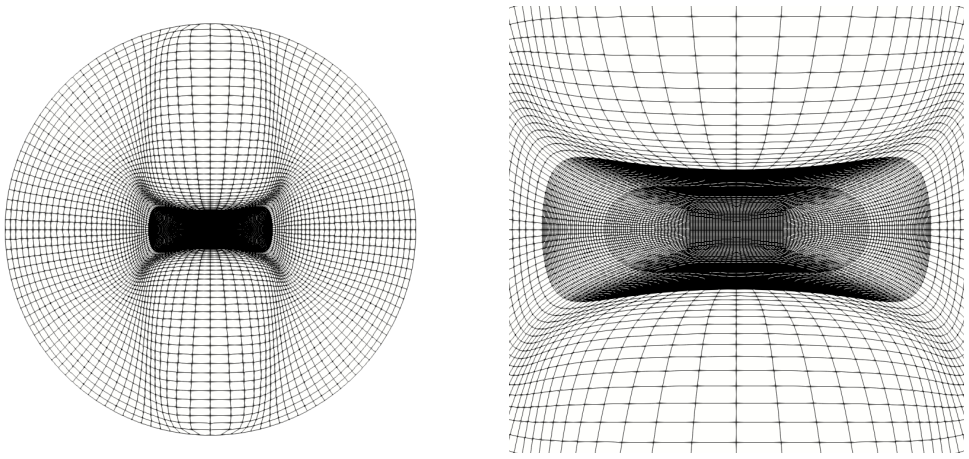

(a) Deformed mesh (b) zoom

Figure 5.4: The deformed mesh (a) obtained with the mapping function δ outlined below. The mesh has a total number of around $370,000$ cells. Additional refinements are a priori enforced around the conducting interface.

deformed via the mapping $\delta = (\delta_x, \delta_y)$. The only restriction we impose is that the boundary of the computational domain is circular so as to preserve the spherical PML

$$\begin{cases} \delta_x = 0.8x(1-\arctan^2(4x))\cdot(1+\exp(-|x|))\cdot\left(1-\dfrac{|x|}{\sqrt{R^2-y^2}}\right)^2, \\ \delta_y = \mp A\sin^2(\pi y^2/RT)\cdot(1+\exp(\mp\rho_i y))\cdot\left(1-\dfrac{|y|}{\sqrt{R^2-x^2}}\right)^2, \end{cases} \tag{5.31}$$

where A is the displacement amplitude, T is the displacement period, and ρ_i is the inner radius of the original mesh. For our purpose, we let $A = 55$ and $T = 15$. The resultant domain is shown in Figure 5.4 and numerical output can be found in Table 5.3(b). In Figure 5.5, we plot the magnitude of hybridized magnetic fields with modal order $m = 4$, with $\varepsilon_r = \varepsilon_{r,1}$ and $\varepsilon_{r,2}$. The conducting interface has been stretched, which induces a stronger plasmon interaction, and in turn, an improved quality factor. From Table 5.3, we observe that the spectrum can be manipulated by changing the geometry and that the relationship between the choice of ε_r and η is not trivial. This presents a potential future research topic for the designing of optical devices.

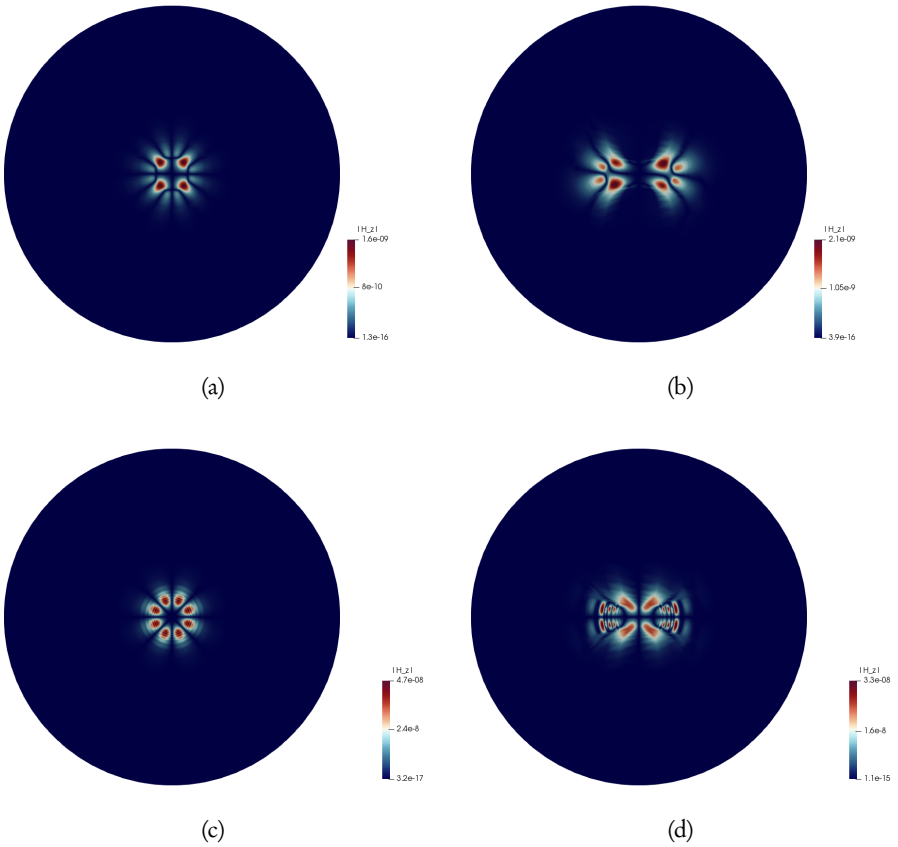

Figure 5.5: An example of $|H_z|$ eigenmode before and after mesh deformation. (a) & (b) are obtained using $\varepsilon_{r,1}$ with modal order of $m = 4$ and (c) & (d) via $\varepsilon_{r,2}$ with $m = 4$.

Chapter 6

Conclusion and Discussion

In this thesis, a numerical framework that simulates wave propagation in the context of optical waveguides is introduced. The main goal of this dissertation is to analyze both numerically and analytically the behavior of the SPPs in the presence of atomically thick conducting interface(s), which can then be utilized to solve a related optimization problem. The primary objective is to quantitatively understand intrinsic properties of waveguides for the design of optimal optical waveguides. The conducting sheets, e.g., graphene, are modeled as idealized hypersurfaces that naturally takes into account the jump condition of the magnetic field.

First, we extended a variational framework for the numerical simulation of the SPPs excited by a current-carrying source on an infinite conducting sheet to the SPPs generated by single/double excitations in a waveguide configuration. We demonstrate that the interlayer coupling of the SPPs present in the two-layer system is responsible for higher confinement and less losses than the single-layer system. We computed optimal interlayer spacings using two approaches. First, we compute via finite element simulations with double-dipole excitation. Second, we derive the pole contribution of the x-directed scattered field solution and solve for the wavenumber of the SPPs (4.15) numerically. The computed values are in agreement with one another. The numerical results on the energy transmission ratio are in very good agreement with analytic results obtained for the SPP mode of the double-layer structure.

The novelty of our study is then presented by allowing more generalized waveguide configuration, i.e., the introduction of gradient-index host. A variational framework is given for the numerical simulation of guided modes with a spatially-dependent dielectric host. This resulted in a quartic eigenvalue problem, in which the electric field and the magnetic field are strongly

coupled. The coupled nonlinear system makes the traditional solving approach difficult to apply and necessitates a new method to simplify to a more familiar format. This is done by linearizing the system via a quadratification approach. Though there are a number of known methods for numerically computing nonlinear eigenvalue problems, such as the FEAST algorithm [29, 30] and within the context of Rayleigh quotient optimization problem [32], this thesis utilizes a more approachable linear algebra tool that is both pragmatic and applicable to a wide range of optical waveguiding problems. The eigenmodes of interest are electromagnetic SPPs that arise on a conducting closed curve, e.g., graphene-coated waveguides.

One of the main advantages offered by our approach is a generalization of material parameters and geometric configuration. We tested our numerical treatment of the quartic eigenvalue problem with analytical predictions in the case of an isotropic medium, and observed excellent agreement. We assessed the relative strength of computed eigenmodes by quantifying eigenvalues via a quality factor, and demonstrated using concrete examples that it is possible to achieve a better quality factor. An improved quality factor is observed for both gradient-index waveguide and generalized geometry.

Our numerics admit several generalizations and extensions. In particular, our variational framework can be readily used without modification to model any geometric configuration that is meshable by quadrilaterals. This flexibility enables numerical simulations of curved waveguides, systems consisting of multiple layers, or complicated optical devices in the near future.

Ideally, we wish to extend our findings in this dissertation to solve the following optimization problem:

$$\begin{aligned} \underset{\varepsilon_r(\boldsymbol{x}),\,\mu_r(\boldsymbol{x}),\,\Sigma}{\text{maximize}} \quad & \frac{\operatorname{Re} k_z(\varepsilon_r(\boldsymbol{x}),\mu_r(\boldsymbol{x}),\Sigma)}{\operatorname{Im} k_z(\varepsilon_r(\boldsymbol{x}),\mu_r(\boldsymbol{x}),\Sigma)} \\ \text{subject to} \quad & [\varepsilon_r]_\Sigma = [\mu_r]_\Sigma = 0, \text{with regularity assumptions,} \\ & l(\Sigma) = c, \text{ where } c \text{ is constant.} \end{aligned}$$

Here, $l(\cdot)$ denotes the length of the conducting interfaces. In the special case where $\varepsilon_r \equiv 1$ and Σ consists of two infinite parallel layers, the optimization problem reduces to one discussed in Section 3. We observe that these generalized constraints can be used as a basis for

solving related shape optimization problems for complicated multilayer optical devices and 3D waveguide designs, which are the subject of potential future research.

Bibliography

[1] J. A. Dionne, L. A. Sweatlock, H. A. Atwater, and A. Polman. Planar metal plasmon waveguides: frequency-dependent dispersion, propagation, localization, and loss beyond the free electron model. *Physical Review B*, 72:075405, 2005.

[2] E. Moreno, F. J. Garcia-Vidal, S. G. Rodrigo, L. Martin-Moreno, and S. I. Bozhevolnyi. Channel plasmon-polaritons: modal shape, dispersion, and losses. *Optical Letters*, 31:3447–3449, 2006.

[3] Q. Li iand M. Qiu. Plasmonic wave propagation in silver nanowires: guiding modes or not? *Optical Express*, 21:8587–8595, 2013.

[4] R. F. Oulton, V. J. Sorger, T. Zentgraf, R-M. Ma, C. Gladden, L. Dai, G. Bartal, and X.Zhang. Plasmon lasers at deep subwavelength scale. *Nature Letters*, 461:629–632, 2009.

[5] C. L. Zou, F. W. Sun, Y. F. Xiao, C. H. Dong, X. D. Chen, J. M. Cui, Q. Gong, Z. F. Han, and G. C. Guo. Plasmon modes of silver nanowire on a silica substrate. *Applied Physics Letters*, 97:183102, 2010.

[6] K. S. Novoselov, S. V. Morozov A. K. Geim, D. Jiang, Y. Zhang, S. V. Dubonos, I. V. Grigorieva, and A. A. Firsov. Electric field effect in atomically thin carbon films. *Science*, 306:666, 2004.

[7] Y. V. Bludov, A. Ferreira, N. M. R. Peres, and M. I. Vasileskiy. A primer on surface plasmon-polaritons in graphene. *International Journal of Modern Physics*, 27(10):1341001, 2013.

[8] J. Liu, X. Zhai, L-L. Wang, H-J. Li, F. Xie, Q. Lin, and S-X. Xia. Analysis of mid-infrared surface plasmon modes in a graphene-based cylindrical hybrid waveguide. *Plasmonics*, 11:703–711, 2016.

[9] A. Vakil and N. Engheta. Transformation optics using graphene. *Science*, 332:1291, 2011.

[10] M. Jablan, H. Bulijan, and M. Soljačič. Plasmonics in graphene at infrared frequencies. *Physical Review B*, 80:245435, 2009.

[11] A. Y. Nikitin, F. Guinea, F. J. García-Vidal, and L. Martín-Moreno. Edge and waveguide terahertz surface plasmon modes in graphene microribbons. *Physical Review B*, 84:161407, 2011.

[12] P. Liu, X. Zhang, Z. Ma, W. Cai, L. Wang, and J. Xu. Surface plasmon modes in graphene wedge and groove waveguides. *Optical Express*, 21:32432–32440, 2013.

[13] Y. Gao, G. Ren, B. Zhu, H. Liu, Y. Lian, and S. Jian. Analytical model for plasmon modes in graphene-coated nanowire. *Optics Express*, 22:24322–24331, 2014.

[14] Y. Gao, G. Ren, B. Zhu, J. Wang, and S. Jian. Single-mode graphene-coated nanowire plasmonic waveguide. *Optics Letters*, 39:5909–5912, 2014.

[15] E. H. Hwang and S. Das Sarma. Plasmon modes of spatially separated double-layer graphene. *Physical Review B*, 80:205405, 2009.

[16] E. H. Hwang, R. Sensarma, and S. Das Sarma. Plasmon-phonon coupling in graphene. *Physical Review B*, 82:195406, 2010.

[17] T. Stauber and G. Gomez-Santos. Plasmons and near-field amplification in double-layer graphene. *Physics Review B*, 85:075410, 2011.

[18] A. H. Castro Neto, F. Guinea, N. M. R Peres, K. S. Novoselov, and A. K. Geim. The electronic properties of graphene. *Reviews of Modern Physcs*, 81:109, 2009.

[19] Z. Fei, G. O. Andreev, W. Bao, L. M. Zhang, A. S. McLeod, C. Wang, M. K. Stewart, Z. Zhao, G. Dominguez, M. Thiemens, M. M. Fogler, M. J. Tauber, A. H. Castro-Neto, C. N. Lau, Keilmann F., and D. N. Basov. Infrared nanoscopy of dirac plasmons at the graphene-SiO_2 interface. *Nano Lett.*, 11:4701, 2011.

[20] L. Ju, B. Geng, J. Horng, C. Girt, M. Martin, Z. Hao, X. Liang H. A. Bechtel, A. Zettl, Y. Ron Shen, and F. Wang. Graphene plasmonics for tunable terahertz metamaterials. *Nature nanotechnology*, 6:630, 2011.

[21] J. Xu, N. Shi, Y. Chen, X. Lu, H. Wei, Y. Lu, N. Liu, B.Zhang, and J.Wang. Tm01 mode in a cylindrical hybrid plasmonic waveguide with large propagation length. *Applied Optics*, 57:4043–4047, 2018.

[22] Y. Xu, Y. Fu, and H. Chen. Planar gradient metamaterials. *Nature Reviews Materials*, 1:16067, 2016.

[23] F. Moharrami and Z. Atlasbaf. Tunable grin lensing based on graphene-dielectric multilayer metamaterials. *Journal of Optics*, 22, 2020.

[24] Q. I. Dai, Y. H. Lo, W. C. Chew, and L. J. Jiang. An efficiently preconditioned eigenanalysis of inhomogeneously loaded rectangular cavities. *IEEE Antennas Wireless Propagation Letters*, 12:58–61, 2013.

[25] Q. I. Dai, W. C. Chew, and L. J. Jiang. Differential forms inspired discretization for finite element analysis of inhomogeneous waveguides. *Progress in Electromagnetics Research*, 143:745–760, 2013.

[26] W. C. Chew. *Waves and Fields in Inhomogeneous Media*. Wiley-IEEE Press, New York, 1999.

[27] D. A. White and J. M. Koning. Computing solenoidal eigenmodes of the vector helmholtz equation: A novel approach. *IEEE Transactions on Magnetics*, 38:3420–3425, 2002.

[28] E. Polizzi. Density-matrix-based algorithms for solving eigenvalue problems. *Physics Review B*, 79:115112, 2009.

[29] B. Gavin, A. Miedlar, and E. Polizzi. Feast eigensolver for nonlinear eigenvalue problems. *Journal of Computational Science*, 27:107–117, 2018.

[30] J. Gopalakrishnan, L. Grubisic, J. Ovall, and B. Q. Parker. Analysis of feast spectral approximations using the dpg discretization. *Computational Methods in Applied Mathematics*, 19:251–266, 2019.

[31] J. Gopalakrishnan, L. Grubisic, and J. Ovall. Spectral discretization errors in filtered subspace iteration. *Mathematics of Computation*, 89:321, 2020.

[32] Z. Bai, D. Lu, and B. Vandereycken. Robust rayleigh quotient minimization and nonlinear eigenvalue problems. *Siam Journal on Scientific Computing*, 40:A3495–A3522, 2018.

[33] M. V. Shuba, G. Y. Slepyan, S. A. Maksimenko, C. Thomsen, and A. Lakhtakia. Theory of multiwall carbon nanotubes as waveguides and antennas in the infrared and the visible regimes. *Physical Review B*, 79:155403, 2009.

[34] G. Beadie, J. N. Mait, R. A. Flynn, and P. Milojkovic. Materials figure of merit for achromatic gradient index (GRIN) optics. *Proc. SPIE 9822*, 2016.

[35] J. Neu, B. Krolla, O. Paul, B. Reinhard, R. Beigang, and M. Rahm. Metamaterial-based gradient index lens with strong focusing in the THz frequency range. *Optics Express*, 18:27748–27757, 2010.

[36] N. Kundtz and D. R. Smith. Extreme-angle broadband metamaterial lens. *Nature Materials*, 9:129–132, 2010.

[37] M. D. Goldflam, T. Driscoll, B. Chapler, O. Khatib, N. M. Jokerst, S. Palit, D. R. Smith, B-J. Kim, G. Seo, H-T. Kim, M. Di Ventra, and D. N. Basov. Reconfigurable gradient index using VO_2 memory metamaterials. *Applied Physics Letters*, 99:044103, 2011.

[38] Q. Fu, F. Zhang, and Y. Fan. Reconfigurable-focus flat lens based on gradient index metamaterials. *Journal of Optics*, 17:085103, 2015.

[39] Y. E. Geints, A. A. Zemlyanov, and E. K. Panina. Photonic nanojet calculations in layered radially inhomogeneous micrometer-sized spherical particles. *Journal of the Optical Society of America B*, 28:1825–1830, 2011.

[40] X. Mao, Y. Yang, H. Dai, D. Luo, B. Yao, and S. Yan. Tunable photonic nanojet formed by generalized Luneburg lens. *Optics Express*, 23:26426–26433, 2015.

[41] C-Y. Liu. Flexible Photonic Nanojet Formed by Cylindrical Graded-Index Lens. *Crystals*, 9:198, 2019.

[42] X. Chen, H. F. Ma, X. Y. Zou, W. X. Jiang, and T. J Cui. Three-dimensional broadband and high-directivity lens antenna made of metamaterials. *Journal of Applied Physics*, 110:044904, 2011.

[43] C. Díaz-Avi nó, M. Naserpour, and C. J. Zapata-Rodriguez. Tunable scattering cancellation of light using anisotropic cylindrical cavities. *Plasmonics*, 12:675–683, 2017.

[44] C. Gomez-Reino, M. V. Perez, C. Bao, and M. T. Flores-Arias. Design of GRIN optical components for coupling and interconnects. *Laser and Photonics Reviews*, 2:203–215, 2008.

[45] S. H. Song, S. Park, C. H. Oh, P. S. Kim, M. H. Cho, and Y. S. Kim. Gradient-index planar optics for optical interconnections. *Optics Letters*, 23:1025–1027, 1998.

[46] V. Pacheco-Pe na, V. Torres, M. Beruete, M. Navarro-Cía, and N. Engheta. ε-near-zero (ENZ) graded index quasi-optical devices: steering and splitting millimeter waves. *Journal of Optics*, 16:094009, 2014.

[47] V. Pachecco-Pe na and M. Beruete. Steering surface plasmons with a graded index dielectric medium. *Journal of Physocs D: Applied Physics*, 51:485101, 2018.

[48] F. De Terán, F. M. Dopico, and D. S. Mackey. Spectral equivalence of matrix polynomials and the index sum theorem. *Linear Algebra and its Applications*, 459, 2014.

[49] Peter Monk. *Finite Element Methods for Maxwell's Equations*. Numerical Mathematics and Scientific Computation. Oxford University Press, 2003.

[50] J. A. Stratton. *Electromagnetic Theory*. McGraw-Hill Book Company, New York, 1941.

[51] D. Margetis and M. Luskin. On solutions of maxwell's equations with dipole sources over a thin conducting film. *Journal of Mathematical Physics*, 57(4), 2016.

[52] M. Maier, D. Margetis, and M. Luskin. Dipole excitation of surface plasmon on a conducting sheet: finite element approximation and validation. *Journal of Computational Physics*, 339:126–145, 2017.

[53] G. W. Hanson. Dyadic green's functions and guided surface waves for a surface conductivity model of graphene. *Journal of Applied Physics*, 103(6):064302, 2008. Erratum, *ibid.* 113(2):029902, 2013.

[54] J.-M. Jin and D. J. Riley. *Finite Element Analysis of Antennas and Arrays*. Wiley, 2009.

[55] M. Maier, D. Margetis, and A. Mellet. Homogenization of time-harmonic Maxwell's equations in nonhomogeneous plasmonic structures. *Journal of Computational and Applied Mathematics*, 2020.

[56] F. Assous and P. Ciarlet Jr. Une charactérisation de l'orthogonal de $\Delta(H^2(\Omega) \cap H_0^1(\Omega))$ dans $L^2(\Omega)$. *Comptes Rendus de l'Académie des Sciences, Paris, S erie 1*, 325:605–610, 1997.

[57] F. Assous, P. Ciarlet Jr., P. A. Raviart, and E. Sonnerdrücker. Characterization of the singular part of the solution of Maxwell's equations in a polyhedral domain. *Math. Meth. Appl. Sci.*, 22:485–499, 1999.

[58] M. Costabel and M. Dauge. A density result for the regularized Maxwell equations in a Lipschitz domain. *Comptes Rendus de l'Académie des Sciences, Paris, S erie 1*, 327:849–854, 1998.

[59] M. Dauge, M. Costabel, and D. Martin. Numerical investigation of a boundary penalization method for Maxwell equations. *Proceedings of the 3rd European Conference on Numerical Mathematics and Advanced Applications*, pages 214–221, 2000.

[60] J. C.Nédélec. Mixed finite elements in $\mathbb{R}^3$. *Numerische Mathematik*, 35:315–341, 1980.

[61] A. Bossavit. *Computational Electromagnetism*. Academic Press, San Diego, 1998.

[62] R. Hiptmair. Finite elements in computational electromagnetism. *Acta Numerica*, 11:237–339, 2002.

[63] D. N. Arnold, R. S. Falk, and R. Winther. Finite element exterior calculus: from hodge theory to numerical stability. *Bulletin of the American Mathematical Society*, 47:281–354, 2010.

[64] B. Wang, X. Zhang, X. Yuan, and J. Teng. Optical coupling of surface plasmons between graphene sheets. *Applied Physics Letters*, 100:131111, 2012.

[65] Choon How Gan Hong Son Chu and Er Ping Li. Synthesis of highly confined surface plasmon modes with doped graphene sheets in the midinfrared and terahertz frequencies. *Physical Review B*, 85:125431, 2012.

[66] E. H. Hwang and S. Das Sarma. Dielectric function, screening, and plasmons in two-dimensional graphene. *Physical Review B*, 75:205418, 2007.

[67] L. A. Falkovsky and S. S. Pershoguba. Optical far-infrared properties of a graphene monolayer and multilayer. *Physics Review B*, 76:153410, 2007.

[68] Kenneth W.-K. Shung. Dielectric function and plasmon structure of stage-1 intercalated graphite. *Physics Review B*, 34:979, 1986.

[69] J.-C.Nédélec. *Acoustic and Electromagnetics Equations*, volume 144 of *Applied Mathematical Sciences*. 2001.

[70] J.-P. Bérenger. A perfectly matched layer for the absorption of electromagnetic waves. *Journal of Computational Physics*, 114:185–200, 1994.

[71] W. C. Chew and W. H. Weedon. A 3d perfectly matched medium from modified maxwell's equations with stretched coordinates. *Microwave and Optical Technology Letters*, 7(13):599–604, 1994.

[72] R. Becker and R. Rannacher. An Optimal Control Approach to A Posteriori Error Estimation in Finite Element Methods. *Acta Numerica*, 10:1–102, 2001.

[73] M. Braack and T. Richter. Solutions of 3D Navier-Stokes Benchmark Problems With Adaptive Finite Elements. *Computers and Fluids*, 35:27–392, 2006.

[74] D. Arndt, W. Bangerth, D. Davydov, T. Heister, L. Heltai, M. Kronbichler, M. Maier, J.-P. Pelteret, B. Turcksin, and D. Wells. The deal.ii finite element library: design, features, and insights. *Computer Methods in Applied Mechanics and Engineering*, 2020. accepted.

[75] D. Arndt, W. Bangerth, T. C. Clevenger, D. Davydov, M. Fehling, D. Garcia-Sanchez, G. Harper, T. Heister, L. Heltai, M. Kronbichler, R. M. Kynch, M. Maier, J.-P. Pelteret, B. Turcksin, and D. Wells. The `deal.II` library, version 9.1. *Journal of Numerical Mathematics*, 2019. accepted.

[76] S. R. J. Brueck. Radiation from a dipole embedded in a dielectric slab. *IEEE Journal on Selected Topics in Quantum Electronics*, 6:899, 2000.

[77] S. Balay, K. Buschelman, V. Eijkhout, W. D. Gropp, D. Kaushik, M. G. Knepley, L. C. McInnes, B. F. Smith, and H. Zhang. PETSc users manual. *Technical Report ANL-95/11 - Revision 2.1.5*, Argonne National Laboratory, 2004.

[78] V. Hernandez, J. E. Roman, and V. Vidal. A scalable and flexible toolkit for the solution of eigenvalue problems. *ACM Transactions on Mathematical Software*, 31, 2005.

[79] F. Collino and P. Monk. The perfectly matched layer in curvilinear coordinates. *SIAM Journal on Scientific Computing*, 19:2061–2090, 1998.

[80] D. S. Mackey, N. Mackey, C. Mehl, and V. Mehrmann. Möbius transformations of matrix polynomials. *Linear Algebra and its Applications*, 470:120–184, 2014.